

Cytoskeletal Control of CD36 Diffusion Promotes Its Receptor and Signaling Function

Khuloud Jaqaman,^{1,2,6} Hirotaka Kuwata,^{3,6} Nicolas Touret,⁴ Richard Collins,³ William S. Trimble,³ Gaudenz Danuser,^{2,5,*} and Sergio Grinstein^{3,*}

¹Department of Systems Biology, Harvard Medical School, Boston, MA 02115, USA

²Department of Cell Biology, The Scripps Research Institute, La Jolla, CA 92037, USA

³Cell Biology Program, The Hospital for Sick Children, Toronto, ON M5G 1X8, Canada

⁴Department of Biochemistry, University of Alberta, Edmonton, AB T6G 2E1, Canada

⁵Department of Cell Biology, Harvard Medical School, Boston, MA 02115, USA

⁶These authors contributed equally to this work

*Correspondence: gaudenz_danuser@hms.harvard.edu (G.D.), sergio.grinstein@sickkids.ca (S.G.)

DOI 10.1016/j.cell.2011.06.049

SUMMARY

The mechanisms that govern receptor coalescence into functional clusters—often a critical step in their stimulation by ligand—are poorly understood. We used single-molecule tracking to investigate the dynamics of CD36, a clustering-responsive receptor that mediates oxidized LDL uptake by macrophages. We found that CD36 motion in the membrane was spatially structured by the cortical cytoskeleton. A subpopulation of receptors diffused within linear confinement regions whose unique geometry simultaneously facilitated freedom of movement along one axis while increasing the effective receptor density. Co-confinement within troughs enhanced the probability of collisions between unligated receptors and promoted their clustering. Cytoskeleton perturbations that inhibited diffusion in linear confinement regions reduced receptor clustering in the absence of ligand and, following ligand addition, suppressed CD36-mediated signaling and internalization. These observations demonstrate a role for the cytoskeleton in controlling signal transduction by structuring receptor diffusion within membrane regions that increase their collision frequency.

INTRODUCTION

Receptor clustering and organization into membrane microdomains is an essential feature of transmembrane signal transduction (Cebecauer et al., 2010; Groves and Kuriyan, 2010; Scott and Pawson, 2009). While receptors were initially thought to cluster upon binding multivalent ligands (Heldin, 1995), there is increasing evidence that receptors can also exist in pre-formed clusters that get reorganized and activated upon ligand binding (Cambi et al., 2006; Chung et al., 2010; Iino et al., 2001; Livnah

et al., 1999; Sako et al., 2000; Schamel et al., 2005; Varma and Mayor, 1998). Membrane microdomains enriched in cholesterol and sphingolipids (Foster et al., 2003; Friedrichson and Kurzchalia, 1998; Hess et al., 2007; Pike, 2003; Sharma et al., 2004), interactions between transmembrane proteins and the cytoskeleton (Andrews et al., 2008; Bouzigues et al., 2007; de Keijzer et al., 2011; Goswami et al., 2008; Kaizuka et al., 2009; Plowman et al., 2005; Serge et al., 2003; Suzuki et al., 2007), and interactions between proteins within the membrane (Douglass and Vale, 2005; Espenel et al., 2008) have been implicated in regulating receptor dynamics and clustering. Very little is known about these emerging mechanisms of unligated receptor clustering and their roles in controlling the signaling competence of receptors.

CD36 is a clustering-responsive class B scavenger receptor expressed on the surface of platelets, endothelial cells, and macrophages (Febbraio et al., 2001). In macrophages, it binds to multivalent ligands such as oxidized low-density lipoprotein (oxLDL), apoptotic cells, and malaria-infected erythrocytes, implicating it in a wide range of processes, from lipid metabolism to innate immunity to tissue remodeling (Endemann et al., 1993; McGilvray et al., 2000; Savill, 1997). Biochemical studies suggest that CD36 clustering at the cell surface upon engagement of multivalent ligands triggers signal transduction and receptor-ligand complex internalization (Daviet et al., 1997; McGilvray et al., 2000). However, it is not known whether unligated CD36 exists as monomers or as clusters that facilitate the cellular response to ligand, and what factors contribute to CD36 clustering. To address these questions, we combined quantitative live-cell single-molecule imaging and immunochemical approaches to study the dynamics, clustering, and signaling of CD36 in primary human macrophages.

RESULTS

Single-Molecule Imaging of CD36 on the Surface of Primary Human Macrophages

To image single receptors, we immunolabeled CD36 with a primary anti-CD36 Fab fragment followed by a secondary Fab

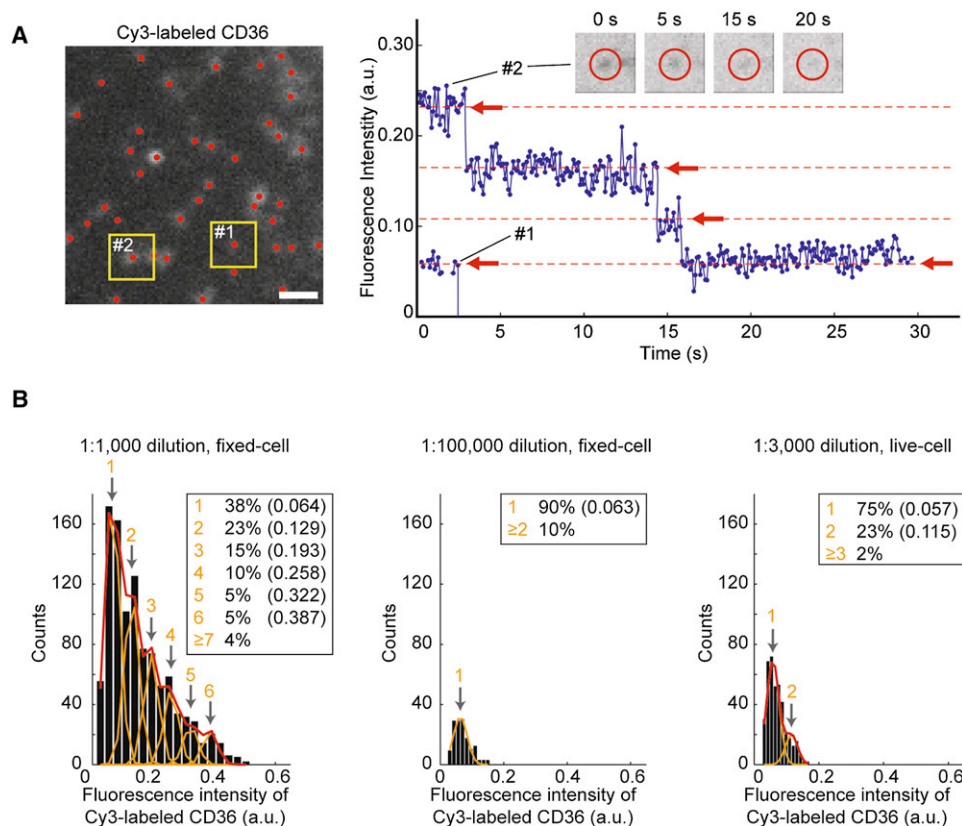


Figure 1. Single-Molecule Imaging of CD36 in Primary Human Macrophages

(A) Single-molecule image (left) and particle fluorescence step photobleaching (right). Particles 1 and 2 are composed of one and four Cy3 molecules, respectively. Scale bar, 1 μm . Insets, representative images of Particle 2.

(B) Fluorescence intensity histograms of detected CD36 particles at different primary Fab fragment dilutions in fixed (left and middle) and live (right) cells, decomposed into individual intensity modes (orange lines, individual modes; red lines, sum of all modes). Arrows show mode centers; numbers indicate the number of Cy3s each mode represents. Insets: Fraction of detected particles in each mode, and mode centers (in parentheses). See also Figure S1.

fragment conjugated largely (>85%) with a single Cy3 fluorophore, and imaged the dorsal surface of macrophages using wide-field epifluorescence microscopy. The resulting images consisted of diffraction-limited spots (Figure 1A), the subpixel positions and peak intensities of which were determined by fitting mixtures of Gaussian kernels (Jaqaman et al., 2008) (see Figure S1A available online).

To assess whether the spots corresponded to single fluorophores, we imaged fixed cells using a range of primary Fab fragment dilutions at a fixed concentration of secondary Fab fragment. Modal analysis of the particle intensity histograms (Yang et al., 2007) revealed multiple intensity modes with conserved mean intensities across all dilutions (Figure 1B). Moreover, individual particles photobleached in a stepwise fashion, with a step size similar to the mean of the first mode in the intensity histograms (Figure 1A). Thus, the first mode of the intensity histograms most likely corresponded to a single Cy3 fluorophore, demonstrating our ability to detect single molecules. Of note, not all secondary Fab fragments were conjugated to exactly one Cy3 and, at the labeling densities used, not every CD36 molecule on the surface was labeled. For these reasons,

the following analysis does not assume that one fluorophore represents one CD36 molecule.

CD36 Exhibits Multiple Motion Types on the Surface of Macrophages

To measure the dynamics of CD36 in live cells, we chose an intermediate labeling density (Figure 1B, right) that balanced the conflicting requirements of tracking single receptors while at the same time capturing interactions between them. Movies were collected with a frame rate of 10 Hz for 10 s (Movie S1, left), over which period photobleaching was negligible (Figures S1B and S1C). Receptor trajectories were reconstructed using a multiple-particle tracking algorithm (Jaqaman et al., 2008) designed to follow individual particles in densely populated fields and to explicitly capture their merging and splitting with other particles (Movie S1, right, and Movie S2).

In unstimulated macrophages CD36 exhibited several trajectory types (Figure 2A), which we classified using two measures: The first characterized trajectories as linear or isotropic based on the scatter of receptor positions regardless of the underlying mobility (Huet et al., 2006; Jaqaman et al., 2008). The second

identified the mobility by a moment scaling spectrum (MSS) analysis of receptor displacements (Ewers et al., 2005; Ferrari et al., 2001) (Figure S2A). The combination of these two measures revealed that $27\% \pm 1\%$ of receptors had linear trajectories, $18\% \pm 1\%$ had isotropic trajectories generated by unconfined diffusion (referred to as isotropic-unconfined), and $55\% \pm 1\%$ had isotropic trajectories generated by confined diffusion (referred to as isotropic confined) (Figure 2B).

The linear trajectories of CD36 radiated from the perinuclear region (Figures 2A and 2C and Figure S2B). Since unligated CD36 is thought to reside exclusively at the cell surface (Collins et al., 2009), this unexpected linear movement raised the possibility that binding to Fab fragments triggered CD36 internalization and displacement along microtubules (MTs). However, following an acute acid wash that preserved cell integrity, only 15% of the fluorescent particles remained (Figures S2C–S2H). This fraction was smaller than the fraction of linearly moving receptors, and none of the remaining label exhibited linear motion (Figure S2F). These results indicated that the majority of the imaged receptors were surface-bound, including those moving linearly.

CD36 Motion along Linear Trajectories Promotes Metastable Clustering

The imaged receptors, even though unligated, underwent merging and splitting events (Figures 2D–2F and Movie S2). These events could be apparent fusions reflecting incidental colocalization of receptors within distances closer than the resolution limit (~ 300 nm), or they could be genuine reversible clustering events formed, for example, through direct interactions between receptors, indirect interactions via other molecules, and/or receptor co-confinement within membrane nanodomains. We used several measures to distinguish genuine clustering from incidental colocalization. First, we compared the measured distribution of fusion times (Figure 2G) to the distribution expected were merging and splitting events solely due to incidental colocalization (Kasai et al., 2011). Specifically, we simulated noninteracting receptors that moved on the cell surface in a manner similar to CD36 and obtained the distribution of apparent fusion times caused by resolution limitations. With this distribution, if the probability of observing a simulated apparent fusion time $\geq X$ s was $p(X)$, then we defined the confidence that an experimental fusion lasting for X s represented a true clustering event as $1 - p(X)$ (Figure 2G). We found that CD36 fusion events could not be accounted for solely by incidental encounters: 60% of the experimentally observed fusions lasted longer than 1 s, the 90% confidence threshold. Second, since a protein's diffusion speed in the membrane is linked to its dimension (Gambin et al., 2006), we investigated whether fused receptors moved slower than before merging or after splitting. We found that 65% of receptors indeed exhibited slower speeds while fused (Figures S2I and S2J). In addition, we found a significant negative cross-correlation between particle intensity and mobility (Figure S2K). These results implied that at least 60%–65% of the observed merging and splitting events reflected genuine reversible clustering events, while the rest were most likely apparent mergers due to resolution limitations.

Even though clustering events were rare overall (Figure 2F), they depended on the type of receptor motion. First, there was a gradient in particle intensities: linearly moving particles had the highest intensity and isotropic-confined particles the lowest (Figure 2H), implying that the chance of a detected particle consisting of multiple CD36 molecules was highest for linearly moving particles, and lowest for isotropic-confined particles. Second, we observed a gradient in the probability of merging and splitting: again linearly moving receptors had the highest probability and isotropic-confined receptors the lowest (Figure 2I). These observations collectively indicated that the linear movement of CD36 favored metastable clustering in the absence of ligand.

CD36 Linear Motion Is Diffusion within Linear Confinement Regions

MSS analysis of the diffusion of linearly moving receptors rarely classified them as super-diffusive (only $\sim 7\%$). To further dissect the linear motion characteristics, we determined the orientation axis of each linear trajectory, defined as the axis of largest positional variation within a trajectory (Figure S2B), and extracted two parameters (Figure 3A): (1) the component of the frame-to-frame displacement parallel to the orientation axis, and (2) the run time, i.e., the number of steps taken in one direction before switching to the opposite direction. We found no difference between motion away from and toward the perinuclear region (Figure 3B). Also, the distribution of run times resembled that of a 1D random walk, where the probability of taking n consecutive steps in one direction is 2^{-n} (Berg, 1993). These results suggested that the linear motion of unligated CD36 was not motor driven but rather diffusive.

To test this hypothesis further, we collected movies with higher sampling frequencies (33, 62.5, and 125 Hz) and compared receptor motion across timescales. For these experiments we labeled CD36 with quantum dots (Qdots) instead of Cy3 because of their brighter and more photostable signal. Qdot blinking was compensated for by the gap-closing feature of the multiple-particle tracking algorithm (Jaqaman et al., 2008). This multiscale analysis yielded several results: First, the mean parallel component of the frame-to-frame displacements scaled with the square root of time, as expected for diffusion (Figure 3C; see also Figure S3A). In contrast, motors would scale linearly with time. Second, as expected for a timescale invariant process such as diffusion (Sethna, 2006), the distributions of run times expressed in frames did not vary with frame rate (Figure 3D). In contrast, motor-driven motion should have a characteristic processivity, in which case frame rate changes would alter the run time distribution expressed in frames. Third, in agreement with the isotropic nature of diffusion, the average receptor displacement component perpendicular to the orientation axis (Figure 3A) was very similar to the average parallel displacement component at 125 Hz sampling (Figure 3C; at lower sampling rates, confinement in the perpendicular direction prevented the full square-root-of-timescaling of the perpendicular component). Fourth, receptors visited all positions within their linear confinement regions, albeit with a bias toward the edges, providing further evidence for motion isotropy (Figure 3E and Figures S3B–S3D). Combined, these observations provided strong evidence

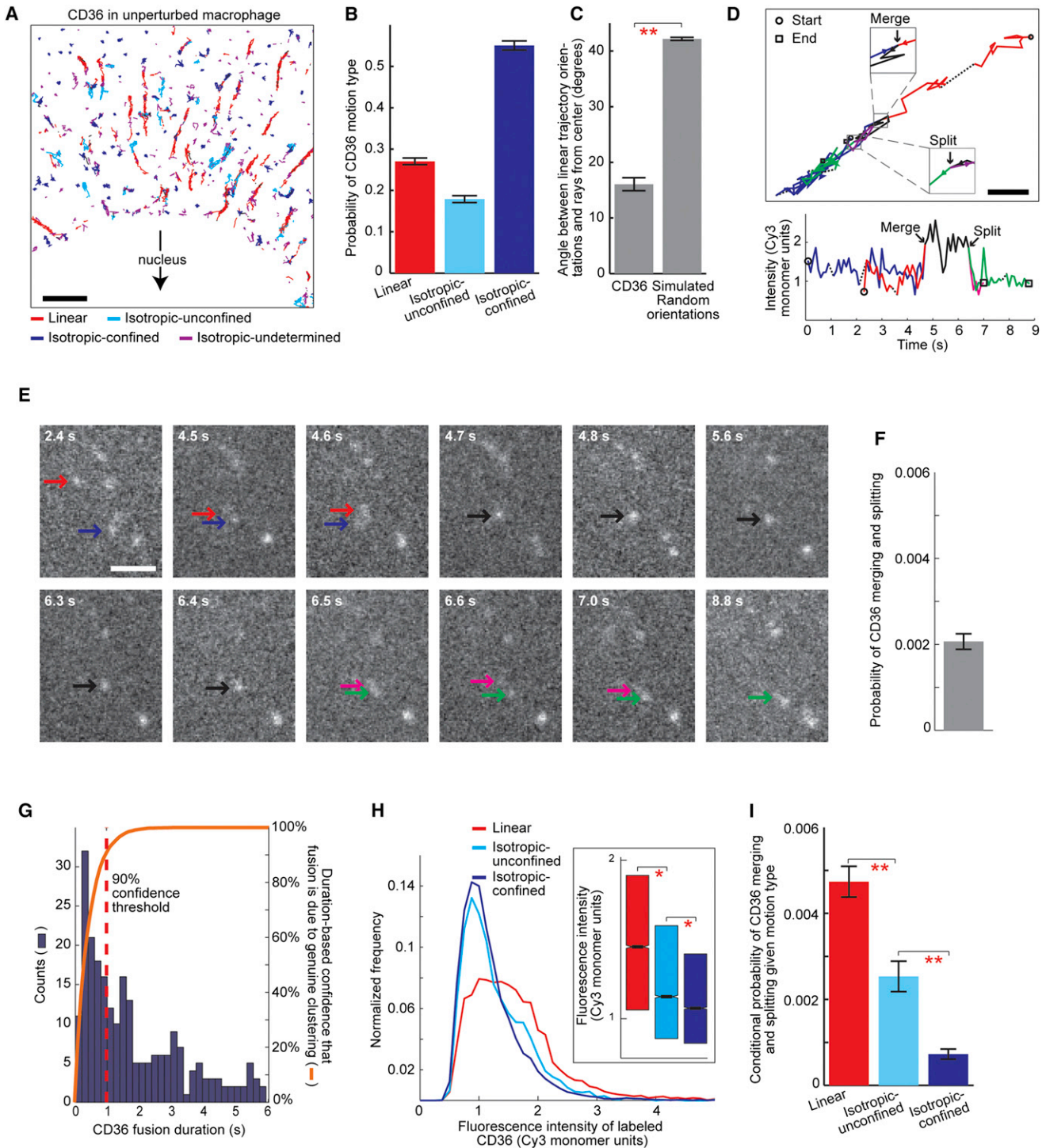


Figure 2. CD36 Moves along Linear Trajectories that Enhance Receptor Clustering

(A) CD36 trajectories in a human macrophage from a 10 Hz/10 s movie (Movie S1). Scale bar, 3 μm . Red, linear trajectories; cyan, isotropic-unconfined trajectories; blue, isotropic-confined trajectories; purple, isotropic-undetermined trajectories, i.e., trajectories that are isotropic but too short for MSS analysis (lasting less than 20 frames). Arrow points to perinuclear region.

(B) Probability of CD36 undergoing the different motion types (from 5455 trajectories in 19 unperturbed cells). Error bars, SEM from 200 bootstrap samples (Efron, 1979).

(C) Mean deviation, in degrees, of the orientation of linear trajectories from a perfect radial arrangement about the perinuclear region. Error bars, SEM from 19 unperturbed cells for CD36 and 20 simulations. **p value < 10^{-4} .

that the linear motion of CD36 on the surface of macrophages resulted from diffusion within linear confinement regions.

The Three Different Motion Types Have Common Features

Differences or similarities between the motion characteristics of the linear, isotropic-unconfined and isotropic-confined receptors could give further insight into the regulation of CD36 motion in the membrane. Thus, we first compared the confinement width of receptors in linear trajectories to the confinement dimension of isotropic-confined receptors. We approximated linear confinement regions by rectangles and isotropic confinement regions by squares. Interestingly, the confinement width of linearly moving receptors and the confinement dimension of isotropic-confined receptors were similar, both with a median of 190 nm (Figures 3E and 3F).

Next, we compared the diffusion coefficient between the three motion categories (Figure 3G). To accommodate the anisotropic geometry of linear trajectories, which caused apparent differences between movements parallel and perpendicular to the orientation axis (Figure 3C), we also calculated for linearly moving receptors their 1D diffusion coefficients parallel and perpendicular to the orientation axis (Figure 3H) (Long and Vu, 2010). The 1D parallel diffusion coefficient was $\sim 0.1 \mu\text{m}^2/\text{s}$, similar to what was previously measured for receptors diffusing freely in the plane of the membrane (Serge et al., 2003). Importantly, the 1D perpendicular diffusion coefficient was similar to the diffusion coefficient of isotropic-confined trajectories, indicating that both motion types were generated by one diffusive movement that was confined within either linear regions or small isotropic regions. The fact that the isotropic-unconfined trajectories had an apparent diffusion coefficient $< 0.1 \mu\text{m}^2/\text{s}$ also suggested that these trajectories did not undergo truly free diffusion but were subject to many short-term constraints unobservable at 10 Hz (Saxton and Jacobson, 1997).

CD36 Linear Motion Does Not Depend on Rafts

CD36 has been reported to localize in the cholesterol-enriched microdomains known as rafts (Dorahy et al., 1996; Zeng et al., 2003). Thus we investigated whether rafts played a role in organizing CD36 motion in the membrane. First we tracked raft dynamics using the raft marker cholera toxin subunit B (CTB) conjugated to Alexa555 (Brown and London, 1998) (Figure S4A). We found that most rafts exhibited isotropic, primarily confined diffusion, although a small fraction exhibited radially arranged linear motion (Figures 4A–4C). Of note, radially arranged linear motion was not a general feature of macrophage membrane

components; $\text{Fc}\gamma$ receptors, for example, did not exhibit any (Figures S4B–S4D). Next, we tracked rafts or CD36 after treating the macrophages with methyl- β -cyclodextrin ($\text{M}\beta\text{CD}$; 10 mM for 30 min) which depleted $\sim 50\%$ of cholesterol from the cells (Figures S4E and S4F). While $\text{M}\beta\text{CD}$ treatment disrupted raft motion as previously reported (Kilsdonk et al., 1995; Ohtani et al., 1989), it had no effect on CD36 motion (Figures 4D and 4E). These results indicated that while some raft-associated molecules could undergo linear motion, the association of CD36 with cholesterol-enriched microdomains was not essential for it to move linearly.

CD36 Linear Motion Depends on the Cortical Actomyosin Meshwork

The actin cytoskeleton has been previously implicated in regulating membrane protein dynamics (Andrews et al., 2008; Chung et al., 2010; Goswami et al., 2008; Kaizuka et al., 2009; Plowman et al., 2005; Suzuki et al., 2007). Therefore, we investigated whether CD36 motion depended on the actin cytoskeleton. Indeed, macrophage treatment with latrunculin B (10 μM for 20 min) to depolymerize F-actin markedly reduced the fraction of linearly moving CD36 (Figures 5A and 5B). These relatively short incubation periods sufficiently preserved the actin cortex to maintain stable cell-substrate adhesion for single-molecule imaging, yet receptor motion was disrupted. Macrophage treatment with blebbistatin (10 μM for 10 min), a specific inhibitor of myosin II, also decreased the fraction of linearly moving receptors (Figures 5A and 5C). Thus, the motion of CD36 in linear confinement regions depended on the integrity and flow of the cortical actomyosin meshwork.

CD36 Linear Motion Depends on MTs

The dependence of CD36 linear motion on the cortical actomyosin meshwork raised the question of what could underlie the formation of the linear structures in the path of CD36. The radial arrangement of the linear trajectories around the nucleus suggested that MTs, closely apposed to the cell cortex in macrophages (Figure S5A), could play a role. Previous studies have implicated MTs in regulating receptor dynamics (Bouzigues et al., 2007; de Keijzer et al., 2011; Serge et al., 2003), although generally resulting in directed movement and not “1D diffusion” as observed for CD36.

Using two-color imaging of Qdot-labeled CD36 and Cy3-immunolabeled MTs in fixed cells, we found a significant fraction of receptors colocalizing with MTs, $27\% \pm 1\%$ (Figures 6A and 6B and Figures S5B–S5D), in remarkable agreement with the fraction of CD36 diffusing within linear confinement

(D) Trajectory and intensity over time of two receptors that merge and then split (Movie S2). Blue and red, trajectories before merging; black, trajectory while fused; magenta and green, trajectories after splitting. Scale bar, 500 nm.

(E) Stills of the receptors whose trajectories are shown in (D). Arrow color coding same as in (D). The two receptors are last detected at time points 7 and 8 s. Scale bar, 2 μm .

(F) Overall probability of labeled CD36 undergoing merging and splitting events. Error bar, SEM from 200 bootstrap samples.

(G) Histogram of measured CD36 fusion durations (blue, left y axis) and duration-based measure of confidence that the fusion events are due to genuine clustering (orange, right y axis), for linearly moving receptors. Similar results were obtained for Brownian receptors (not shown). This analysis was not possible for confined receptors.

(H) Intensity distributions of particles per motion type. Inset: box plots showing second quartile, median and third quartile. *Median comparison p value < 0.05 .

(I) Conditional probability of CD36 merging and splitting per motion type. Error bars, SEM from 200 bootstrap samples. **p $< 10^{-4}$.

See also Figure S2.

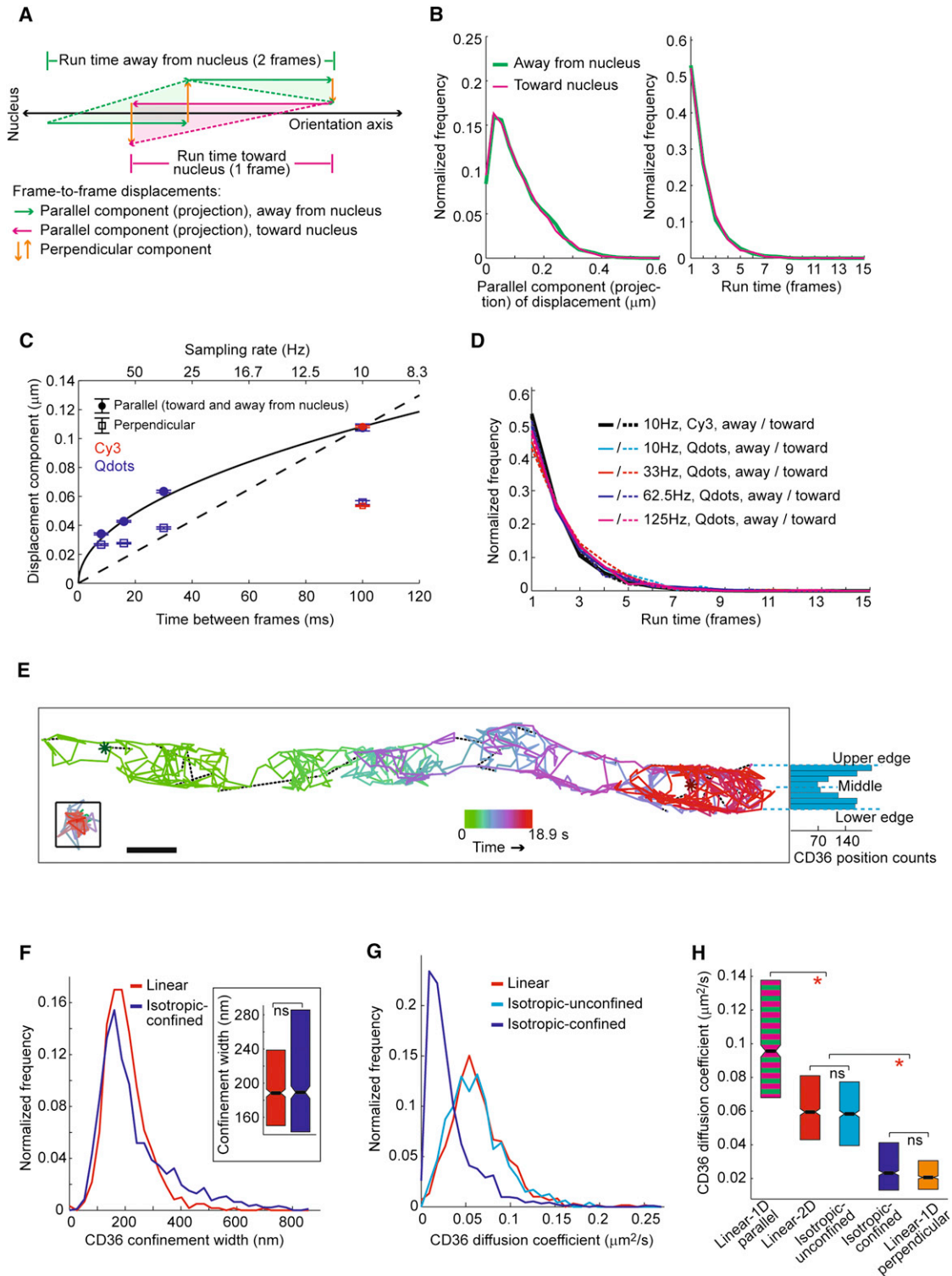


Figure 3. CD36 Linear Motion Is Diffusion within Linear Confinement Regions

(A) Illustration of run time and frame-to-frame displacement decomposition into parallel and perpendicular components. (B) Distribution of frame-to-frame displacement parallel components and run times toward and away from the perinuclear region. (C) Mean magnitude of frame-to-frame displacement parallel (filled circles) and perpendicular (open squares) components at different sampling rates. Error bars, SEM from >1500 data points per sampling rate. Upper x axis, sampling rates; lower x axis, corresponding time between frames. Dashed line, linear scaling of parallel displacement with time; solid line, square root scaling with time. Red symbols, Cy3 data; blue symbols, Qdot data.

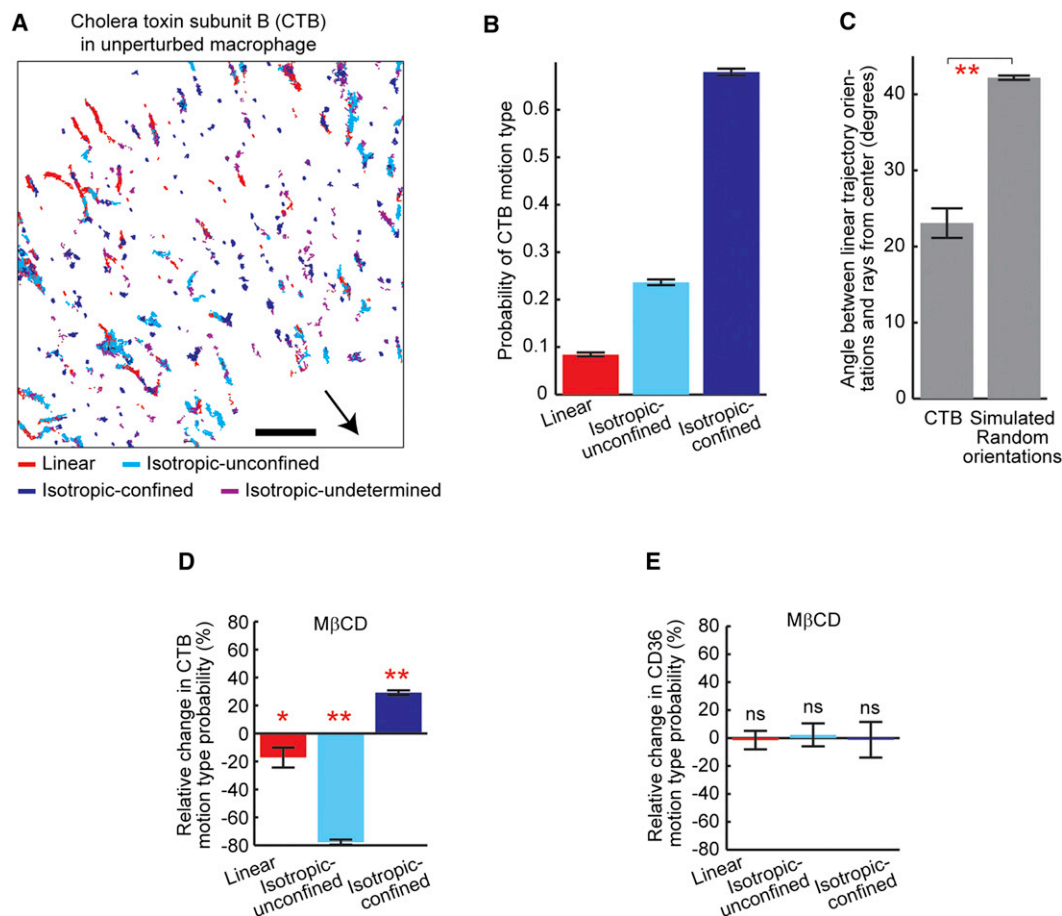


Figure 4. CD36 Linear Motion Does Not Depend on Rafts

(A) Alexa555-conjugated CTB trajectories in a primary human macrophage from a 10 Hz/10 s movie. Trajectory color coding and arrow as in Figure 2A. Scale bar, 3 μ m.

(B) Probability of CTB undergoing the different motion types (from 14,805 trajectories in 23 unperturbed cells). Error bars, SEM from 200 bootstrap samples.

(C) Mean deviation, in degrees, of the orientation of linear trajectories from a perfect radial arrangement about the perinuclear region. Error bars, SEM from 23 unperturbed cells for CTB and 20 simulations. **p value < 10^{-4} .

(D and E) Relative change in CTB (D) and CD36 (E) motion type probabilities after treatment with M β CD in comparison to unperturbed cells (from 6719 trajectories in 22 M β CD-treated cells for CTB and 1603 trajectories in ten M β CD-treated cells for CD36). Error bars, SEM from 200 bootstrap samples. *, **, ns: changes associated with $p < 0.05$, $p < 10^{-4}$, and $p > 0.1$, respectively.

See also Figure S4.

regions (Figure 2B). Live-cell imaging of Qdot-labeled CD36 in macrophages transduced with baculovirus to express tubulin-GFP revealed that linear CD36 trajectories primarily colocalized with MTs (Figure 6C), and were more abundant in areas where MTs were more organized (right versus left side

of cell in Figure 6D). Consistent with these observations, macrophage treatment with nocodazole (50 μ M for 30 min) to depolymerize MTs significantly decreased the fraction of receptors undergoing linear motion (Figures 6E and 6F). Therefore, in addition to the cortical actomyosin meshwork, MTs

(D) Distributions of run times, in frames, at the indicated sampling rates.

(E) Linear CD36 trajectory from a 62.5 Hz/18.9 s (1184 frame) movie of Qdot-labeled CD36, color-coded based on time (green to blue to red). Scale bar, 200 nm. Inset, isotropic-confined trajectory. Inset box size, 200 \times 200 nm. Histogram (right, in cyan): distribution of receptor positions across the width of the linear trajectory.

(F) Distribution of confinement widths for linear and isotropic-confined trajectories. Inset: box plots showing the second quartile, median and third quartile. ns, median comparison p value > 0.05.

(G) Distribution of 2D diffusion coefficients for different motion types.

(H) Box plots showing the second quartile, median and third quartile of the 2D diffusion coefficients shown in (G) and of the 1D diffusion coefficients parallel and perpendicular to the orientation axis of linear trajectories. The 1D parallel diffusion coefficient is shown in magenta and green stripes (colors used in A) to indicate that it includes movement both toward and away from the perinuclear region. *, ns: median comparison $p < 0.05$ and $p > 0.05$, respectively.

See also Figure S3.

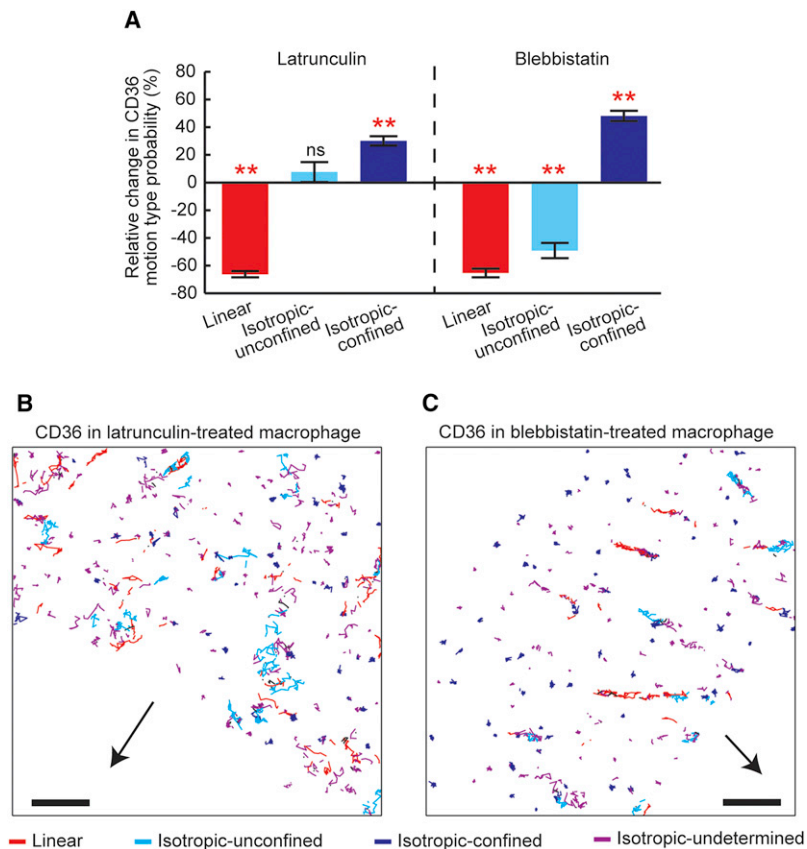


Figure 5. CD36 Linear Motion Depends on the Cortical Actomyosin Meshwork

(A) Relative change in CD36 motion type probabilities after treatment with latrunculin or blebbistatin in comparison to unperturbed cells (from 4886 trajectories in 20 latrunculin-treated cells and 2588 trajectories in 12 blebbistatin-treated cells). Error bars, SEM from 200 bootstrap samples. *, **, ns: changes associated with $p < 0.05$, $p < 10^{-4}$ and $p > 0.1$, respectively.

(B and C) CD36 trajectories after treatment with latrunculin (B) or blebbistatin (C) from 10 Hz/10 s movies. Trajectory color coding and arrow as in Figure 2A. Scale bar, 3 μm . See also Figure S7.

also played a role in mediating the radially arranged linear motion of CD36.

Motion Changes upon Cytoskeleton Perturbation Reduce CD36 Clustering

The propensity of unligated CD36 to form metastable clusters depended on its mobility (Figures 2H and 2I). Thus, we suspected that cytoskeleton perturbations that altered CD36 motion would also perturb its clustering. To investigate this, we compared clustering in the different conditions using two measures: (1) modal analysis of the particle intensity histograms (similar to Figure 1B) and (2) the probability of receptor merging and splitting (similar to Figure 2F). At face value, all drug treatments reduced receptor clustering, with nocodazole showing the weakest reduction (Figures 7A and 7B). However, in addition to altering receptor motion, these drug treatments reduced receptor density on the cell surface (Figure 7C). To separate the effects of motion perturbation and density reduction, we repeated the clustering comparisons between conditions using a subset of cells (called “density-normalized subset”) that had comparable receptor densities (Figures 7D and 7E). In this subset, latrunculin and blebbistatin treatments reduced clustering to a similar extent as they did in all cells, implying that motion changes upon these treatments were the dominant factor in reducing receptor clustering. The effects of nocodazole on the density-normalized subset were not significant, implying that with this drug the reduction in receptor density was more likely

the cause of decreased receptor clustering. Overall, this analysis provided evidence that clustering of unligated CD36 was regulated by geometric constraints mediated by cortical cytoskeleton organization.

Cytoskeleton Perturbation Inhibits CD36 Function and Signaling

Biochemical evidence suggests that CD36 clustering is essential for its signaling and internalization upon engagement to multivalent ligands (Daviet et al., 1997; McGilvray et al., 2000). The metastable clustering of unligated CD36 might prime the cell and facilitate its response when exposed to ligand that, in turn, could stabilize the clusters and/or increase their

size, leading to receptor activation. Our observation that CD36 diffusion within linear confinement regions promoted unengaged receptor clustering thus led us to hypothesize that the cytoskeleton-mediated organization of receptor diffusion in the membrane might enhance CD36 responsiveness to ligand.

To test this, we monitored the response of macrophages to oxLDL, a physiologically important ligand that binds to macrophages largely via CD36 (Figure S6A). We monitored the internalization of oxLDL and the activation of c-Jun N-terminal kinase (JNK), a well-established effector of CD36 (Kennedy et al., 2011; Rahaman et al., 2006).

In unperturbed macrophages, Dil-labeled oxLDL bound rapidly to the surface. Within 5 min of Dil-oxLDL addition, a fraction of the receptor-ligand complexes, $25\% \pm 2\%$, moved along linear trajectories as described for CD36 (Figures 7F and 7G). This behavior was observed before any significant internalization occurred, as verified by acid-stripping the cells, which removed most of the bound oxLDL and eliminated most of the linearly moving complexes (Figure 7G). After 20 min of oxLDL addition, $\sim 60\%$ of the oxLDL was internalized and could no longer be displaced from the cells by an acid wash (data not shown). Binding and internalization of oxLDL were associated with JNK activation, as assessed using antibodies that specifically recognized the phosphorylated form of its substrate cJun (phospho-cJun; Figure 7H and Figure S6B).

To assess the effect of perturbing CD36 motion and clustering on its ability to signal and internalize oxLDL, we pretreated the

cells with latrunculin, blebbistatin or nocodazole before adding oxLDL. Pretreatment with all three agents reduced ligand internalization (Figure 7I), in all cases to a larger extent than what would be expected from the reduction in receptor density alone (Table S1). This reduction did not result from wholesale inhibition of endocytosis, as the same drug treatments did not significantly alter transferrin internalization (Figure 7J). Pretreatment with blebbistatin or nocodazole also suppressed c-Jun phosphorylation (Figure 7H and Figure S6B). The effect of latrunculin on CD36-mediated JNK activation could not be evaluated; as described in other systems (Subbaramaiah et al., 2000; Yujiri et al., 1999), actin-perturbation itself markedly activated JNK, precluding subsequent stimulation via CD36 (Figure 7H; Figure S6B). The results of these experiments combined thus supported the hypothesis that the cytoskeleton-mediated organization of CD36 diffusion was essential for its proper signaling and ability to internalize ligands.

DISCUSSION

CD36 Diffusion in the Membrane Is Spatially Organized by the Cortical Cytoskeleton

Our study reveals that the diffusion of CD36 in the membrane of human macrophages is regulated by interactions between CD36 and the cytoskeleton. Indeed, Triton extraction experiments provide evidence that in macrophages CD36 interacts with F-actin (Figure S7), although most likely transiently and indirectly, perhaps via integrins (Thorne et al., 2000). It is tempting to speculate that some lipid microdomains exhibit radially arranged linear motion like CD36 because of similar interactions with F-actin (Harder et al., 1997; Viola and Gupta, 2007).

While details of the molecular mechanism by which the cytoskeleton controls CD36 diffusion in the membrane remain to be determined, our current data suggest two models: in regions without MTs, the submembranous actin meshwork is isotropic; thus receptors diffuse isotropically and, due to CD36-actin interactions, would get slowed down (Saxton and Jacobson, 1997) and often confined. On the other hand, where MTs are apposed to the membrane (Manneville et al., 2003), they might disrupt the integrity of the submembranous actomyosin meshwork by chemical and/or mechanical interactions (Rodriguez et al., 2003), generating actin-delimited channels along which CD36 would move relatively unobstructed (model 1 in Figure S5E). Alternatively, the submembranous actin meshwork is isotropic everywhere, including regions with MTs, however MTs might locally detach the actin meshwork from the plasmalemma, generating linear patches of bare membrane where receptor diffusion is unimpeded by actin (model 2 in Figure S5E). The remarkable conservation of confinement width between isotropic compartments and linear channels favors the first model. In either case, the reversible interactions between CD36 and F-actin would lead to the observed bias of CD36 localization toward the channel edges (Figure 3E).

The compartmentalization of CD36 diffusion in the membrane is reminiscent of the membrane matrix corrals proposed by Kusumi et al. (2005a, 2005b). However, there are two main differences between CD36 compartments and those described previously. First, for CD36 we observe not only isotropic

compartments but also linear channels. Second, the confinement of CD36 seems to be more long-lived than the previously observed corrals (at least 10 s versus 1 ms timescale [Kusumi et al., 2005a]). Of note, cortical actin turnover is also on the order of tens of seconds (McGrath et al., 1998; Ponti et al., 2005). Therefore, we propose that the linear and isotropic compartments described here are salient features of the cortical architecture in macrophages, controlling receptor diffusion over long periods and thus having major implications for the steady-state of CD36-mediated signal transduction.

The Spatial Organization of CD36 Diffusion in the Membrane Enhances Signal Transduction

A critical implication of the compartmentalization of CD36 diffusion is its impact on receptor interactions. In particular, our data show that CD36 diffusion in linear channels promotes receptor encounters and clustering, which can be attributed to the unique geometry of linear channels: when compared with the small regions of isotropic confinement, the comparatively long linear channels accommodate more receptors and offer them greater freedom of movement parallel to the orientation axis. Conversely, when compared to free diffusion, linear channels restrict movement perpendicular to the orientation axis, thereby increasing the effective local density by approximately 5-fold.

While the exact molecular nature of the CD36 clusters remains to be determined, our study provides evidence that the metastable clusters of unligated CD36 prime the cell to respond when exposed to multivalent ligands. At present the link between cytoskeleton organization and signaling could be probed only by global disruption of actin and MT dynamics. Thus we cannot formally exclude that effects besides reduced receptor clustering contribute to the documented shifts in signaling downstream of CD36. However, the fact that cytoskeleton perturbants working via different molecular mechanisms had similar effects on CD36 function provides compelling evidence that reducing unligated CD36 clustering—common among all the perturbants—is a major contributor to the inhibition of CD36 function upon disruption of cytoskeleton organization.

In conclusion, by dictating the spatial organization of receptor motion, cortical cytoskeletal structures appear to play a critical role in CD36 signal transduction, where the outside-in activation of pathways that modulate cellular processes is in turn controlled by inside-out feedback regulating receptor clustering. We speculate that this reciprocal interaction may be a general mechanism for enhancing or silencing signals at the level of the plasma membrane.

EXPERIMENTAL PROCEDURES

Macrophage Isolation and Culture

Human blood samples from healthy volunteers were collected with heparin. Peripheral blood mononuclear cells were isolated by density-gradient centrifugation using Ficoll-Paque Plus (Amersham). Cells were resuspended (10^7 cells/ml) in RPMI-1640 with L-glutamine containing 10% heat-inactivated fetal calf serum (FCS; from Wisent) and seeded onto 18 mm glass coverslips (Fisher Scientific) at 5×10^5 cells/coverslip. After 1 hr at 37°C, nonadherent cells were removed by multiple washes with Hank's buffered saline solution (HBSS). Adherent cells were incubated in RPMI-1640 with 10% FCS and

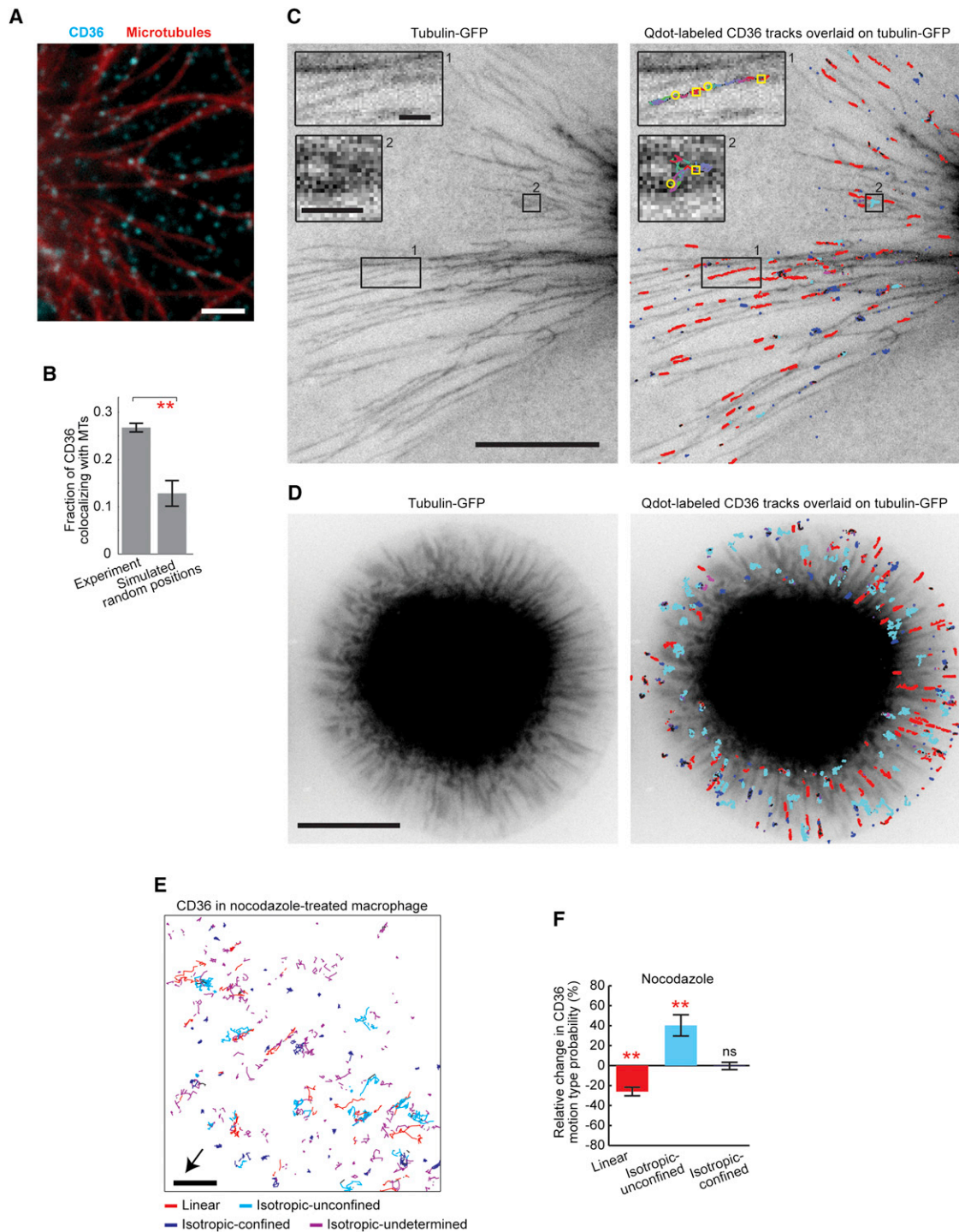


Figure 6. CD36 Linear Motion Depends on MTs

(A) Fixed-cell image overlaying Qdot-labeled CD36 (cyan) and Cy3-immunolabeled MTs (red). Scale bar, 3 μ m.

(B) Fraction of CD36 particles colocalizing with MTs in experimental data, and simulated fraction of colocalization for a random distribution of the same number of particles. Experimental fraction calculated from three images. Error bars, SEM from three experiments and associated simulations. **p value < 10^{-4} .

(C and D) Live-cell images overlaying CD36 trajectories (CD36 tracked using Qdot labeling) and tubulin-GFP, from 10 Hz/14 s movies. Scale bars, 10 μ m. CD36 trajectories are color-coded based on motion type, as in Figure 2A. Insets in (C): Zoom-in on two areas highlighting the colocalization of CD36 trajectories and MTs (see also Movies S3 and S4). Trajectories in insets color-coded based on time (green to blue to red). Yellow circles and squares indicate, respectively, the first and last time points in each trajectory. Scale bars in insets, 1 μ m.

100 U/ml penicillin, 100 µg/ml streptomycin and 10 µg/ml polymyxin B (Invitrogen) for 7–14 days.

CD36 Immunolabeling

Monoclonal antibodies to human CD36 (clone 131.1; mouse IgG₁) were the gift of Dr. N. Tandon (Otsuka America Pharmaceutical, Inc., Rockville, MD). Monovalent Fab fragments were prepared using the ImmunoPure Fab Preparation Kit (Pierce). To minimize nonspecific binding, cells were blocked with 4% donkey serum for 10 min, then incubated with anti-CD36 Fab fragments at 1:2000–1:3000 dilution for 10 min. After washing with HBSS, cells were incubated with either (1) Cy3-conjugated donkey anti-mouse Fab fragments (Jackson ImmunoResearch Laboratories) at a 1:3000 dilution for 10 min; (2) Qdot 655-goat F(ab')₂ anti-mouse IgG conjugates at 1:2000–1:3000 dilution for 10–15 min (to prevent crosslinking, unoccupied antibody-binding sites on the Qdots were blocked with nonimmune mouse IgG antibody [10 µg/ml]); or (3) biotinylated secondary Fab (1:1000 dilution) followed by streptavidin-655 Qdots (1:10,000 dilution); medium with excess free biotin was then added to block sites on avidin, thereby preventing crosslinking. All labeling protocols led to comparable results.

All of the preceding steps were performed at 4°C to minimize lateral mobility and clustering. Cells were then warmed to 37°C before filming.

Other Labeling

To visualize cell-associated oxLDL, cells were labeled with Dil-oxLDL (1:1000) for 5 min and washed with HBSS. To visualize rafts, cells were labeled with 0.5 µg/ml AlexaFluor 555-conjugated CTB for 10 min on ice.

Image Acquisition

Live-cell imaging was performed using a Zeiss Axiovert 200 epifluorescence microscope equipped with a 100× oil-immersion objective (NA 1.45), a custom-made 2.5× lens and either a Cy3 filter set or a 32012 cube from Chroma Technology for Qdots. Illumination was provided by an Exfo X-Cite 120 light source, and a Hamamatsu 9100-13 deep-cooled EM-CCD camera was used for recording. Image acquisition was controlled by Volocity (Perkin-Elmer). Images were acquired continuously at 10, 33, 62.5, and 125 frames per second for 10–20 s.

Acid-Stripping Protocol

To strip anti-CD36 antibodies, oxLDL, transferrin, or CTB bound extracellularly, cells were incubated with 200 mM acetic acid and 150 mM NaCl (pH 2.8) for 5 min at 37°C. Acid stripping was terminated by transferring the cells to prewarmed medium RPMI 1640 buffered with HEPES.

Transferrin and oxLDL Uptake Assays

Primary human macrophages (7–10 days old) were serum-starved in HEPES-buffered RPMI (Wisent Inc.) for 1 hr, treated with or without latrunculin B, blebbistatin or nocodazole followed by addition of either 25 µg/ml transferrin Alexa Fluor-555 conjugate (Molecular Probes) for 30 min at 37°C or 50 µg/ml Dil-oxLDL for 20 min at 37°C. Cells were then acid-washed to remove extracellular adherent ligand and fixed in 4% paraformaldehyde. The amount of cell-associated ligand remaining (i.e., internalized) was quantified by acquiring epifluorescence images that were analyzed using ImageJ software.

Phospho-cJun Assay

To quantify JNK activation, the cells were serum-starved for 3 hr and treated with the indicated cytoskeleton perturbants and/or oxLDL. The cells were then fixed, permeabilized, and immunostained with phospho-cJun antibodies (1:200) followed by Cy3-labeled secondary and counterstained with DAPI. Images were acquired by epifluorescence and quantified using ImageJ. All experiments were performed in triplicate, with at least 50 cells analyzed per experiment.

Microtubule Visualization

To visualize microtubules in fixed cells, cells were treated with methanol for 2 min at –20°C, rinsed, and incubated with monoclonal Cy3-conjugated anti-β tubulin antibody (TUB 2.1). To visualize microtubules in live cells, macrophages (≈30% confluent) were incubated with 400 CellLight Tubulin-GFP BacMam 2.0 baculovirus particles per cell for 16 hr at 37°C and visualized by epifluorescence with the same system used for single-particle tracking.

Particle Tracking

The imaged molecules were detected and tracked as described in (Jaqaman et al., 2008). In brief, particle subpixel positions and intensities—which were subresolution features even for receptor clusters—were estimated by (1) detecting significant local intensity maxima and (2) fitting Gaussian kernels approximating the two-dimensional point spread function of the microscope. Importantly, our algorithm fitted multiple Gaussians simultaneously (i.e., Gaussian mixture-models) for particles with overlapping signals, enhancing the accuracy and resolution of the detection.

The detected particles were tracked using a two step particle tracking algorithm that could follow dense receptor fields and generate complete trajectories by closing gaps and capturing merging and splitting events. In the first step, the algorithm linked particles between consecutive frames by determining the globally optimal set of spatial assignments among all possible assignments between particle pairs. The tracks generated in this step started and ended not only because of true particle appearance and disappearance, but also because of temporary particle disappearance, merging, and splitting. Thus, in the second step, the algorithm generated complete particle trajectories by linking the track segments from the first step in three ways: end-to-start, to close gaps resulting from temporary particle disappearance; end-to-middle, to capture particle merging events; and middle-to-start, to capture particle splitting events. In this step, all track segments were allowed to compete with each other, resulting in a spatially and temporally optimal global assignment of track pairs, adding stability to the tracker under high particle density conditions. The cost functions employed to weigh competing particle and track segment assignments were based on distance and intensity, as well as on motion models that aided tracking by allowing particle position propagation via the Kalman filter. All movies were analyzed using the same tracking parameters. Tracks lasting at least five frames were retained for trajectory analysis.

Trajectory Analysis

Two measures were used to identify and characterize trajectory types: The first classified trajectory shape based on the degree of anisotropy of the scatter of particle positions along a trajectory (Huet et al., 2006; Jaqaman et al., 2008). The second extracted diffusion types using an MSS analysis of particle displacements (Ewers et al., 2005; Ferrari et al., 2001). The MSS analysis was applied to full 2D displacements and to 1D displacements in linear trajectories. Particle diffusion coefficients were calculated from the MSS analysis. The confinement dimension for confined and linear trajectories was derived via eigenvalue decomposition of the variance-covariance matrix of particle positions along each trajectory.

The radial arrangement of linear trajectories around the perinuclear region of a cell was quantified by calculating for each linear trajectory the angle between its orientation axis and the ray connecting the “cell center” to the trajectory center, and averaging the angle over all linear trajectories in the cell.

Please see [Extended Experimental Procedures](#) for a full description of these analysis methods.

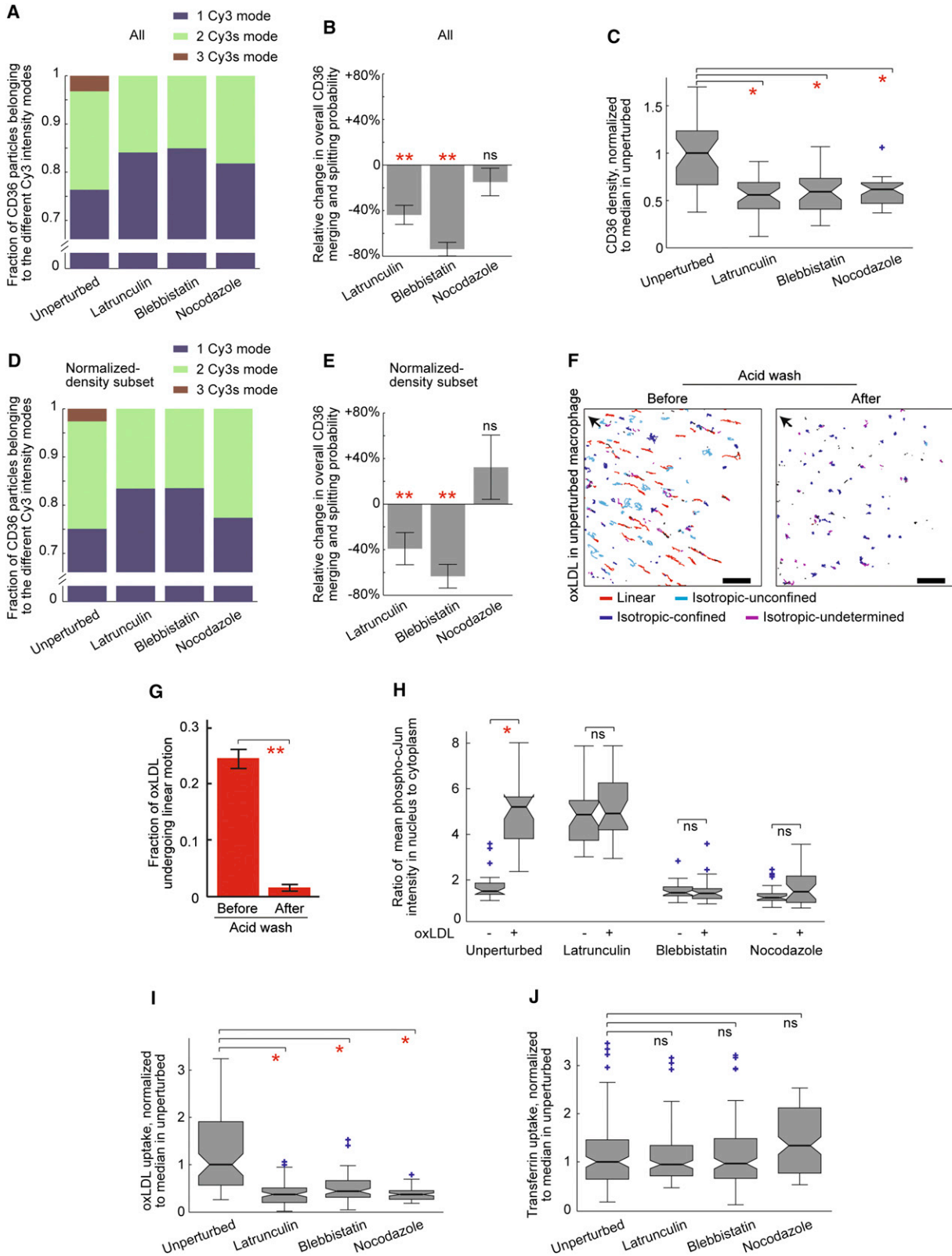
Other Methods

Please see [Extended Experimental Procedures](#) for reagents, immunolabeling controls, measuring cholesterol content and quantifying cytoskeleton-associated CD36; also for a detailed description of apparent fusion time simulations and receptor density estimation.

(E) CD36 trajectories in a nocodazole-treated cell from a 10 Hz/10 s movie. Trajectory color coding and arrow as in [Figure 2A](#). Scale bar, 3 µm.

(F) Relative change in CD36 motion type probabilities after treatment with nocodazole in comparison to unperturbed cells (from 2849 trajectories in 16 nocodazole-treated cells). Error bars, SEM from 200 bootstrap samples. **, ns: changes associated with $p < 10^{-4}$ and $p > 0.1$, respectively.

See also [Figure S5](#).



SUPPLEMENTAL INFORMATION

Supplemental Information includes Extended Experimental Procedures, seven figures, four movies, and one table and can be found with this article online at [doi:10.1016/j.cell.2011.06.049](https://doi.org/10.1016/j.cell.2011.06.049).

ACKNOWLEDGMENTS

Work in the Grinstein lab was supported by the Heart and Stroke Foundation of Ontario and by Canadian Institutes of Health Research Grant MOP-102474. Work in the Danuser lab was supported by NIH grant U01 GM67230. K.J. is an investigator in the Center for Cell Decision Processes (NIH P50 GM068762). HK was supported in part by the Uehara Memorial Foundation, the Mochida Memorial Foundation for Medical and Pharmaceutical Research and the Kanae Foundation for the Promotion of Medical Science. N.T. is supported by an Alberta Heritage Foundation for Medical Research Scholarship. S.G. is the current holder of the Pitblado Chair in Cell Biology.

Received: September 1, 2010

Revised: April 28, 2011

Accepted: June 21, 2011

Published: August 18, 2011

REFERENCES

- Andrews, N.L., Lidke, K.A., Pfeiffer, J.R., Burns, A.R., Wilson, B.S., Oliver, J.M., and Lidke, D.S. (2008). Actin restricts FcεRI diffusion and facilitates antigen-induced receptor immobilization. *Nat. Cell Biol.* **10**, 955–963.
- Berg, H.C. (1993). *Random Walks in Biology* (Princeton, NJ: Princeton University Press).
- Bouziques, C., Morel, M., Triller, A., and Dahan, M. (2007). Asymmetric redistribution of GABA receptors during GABA gradient sensing by nerve growth cones analyzed by single quantum dot imaging. *Proc. Natl. Acad. Sci. USA* **104**, 11251–11256.
- Brown, D.A., and London, E. (1998). Functions of lipid rafts in biological membranes. *Annu. Rev. Cell Dev. Biol.* **14**, 111–136.
- Cambi, A., Joosten, B., Koopman, M., de Lange, F., Beeren, I., Torensma, R., Franssen, J.A., Garcia-Parajó, M., van Leeuwen, F.N., and Figdor, C.G. (2006). Organization of the integrin LFA-1 in nanoclusters regulates its activity. *Mol. Biol. Cell* **17**, 4270–4281.
- Cebecauer, M., Spitaler, M., Sergé, A., and Magee, A.I. (2010). Signalling complexes and clusters: functional advantages and methodological hurdles. *J. Cell Sci.* **123**, 309–320.
- Chung, I., Akita, R., Vandlen, R., Toomre, D., Schlessinger, J., and Mellman, I. (2010). Spatial control of EGF receptor activation by reversible dimerization on living cells. *Nature* **464**, 783–787.
- Collins, R.F., Touret, N., Kuwata, H., Tandon, N.N., Grinstein, S., and Trimble, W.S. (2009). Uptake of oxidized low density lipoprotein by CD36 occurs by an actin-dependent pathway distinct from macropinocytosis. *J. Biol. Chem.* **284**, 30288–30297.
- Daviet, L., Malvoisin, E., Wild, T.F., and McGregor, J.L. (1997). Thrombospondin induces dimerization of membrane-bound, but not soluble CD36. *Thromb. Haemost.* **78**, 897–901.
- de Keijzer, S., Galloway, J., Harms, G.S., Devreotes, P.N., and Iglesias, P.A. (2011). Disrupting microtubule network immobilizes amoeboid chemotactic receptor in the plasma membrane. *Biochim. Biophys. Acta* **1808**, 1701–1708.
- Dorahy, D.J., Lincz, L.F., Meldrum, C.J., and Burns, G.F. (1996). Biochemical isolation of a membrane microdomain from resting platelets highly enriched in the plasma membrane glycoprotein CD36. *Biochem. J.* **319**, 67–72.
- Douglass, A.D., and Vale, R.D. (2005). Single-molecule microscopy reveals plasma membrane microdomains created by protein-protein networks that exclude or trap signaling molecules in T cells. *Cell* **121**, 937–950.
- Efron, B. (1979). Bootstrap methods: another look at the jackknife. *Ann. Stat.* **7**, 1–26.
- Endemann, G., Stanton, L.W., Madden, K.S., Bryant, C.M., White, R.T., and Protter, A.A. (1993). CD36 is a receptor for oxidized low density lipoprotein. *J. Biol. Chem.* **268**, 11811–11816.
- Espenel, C., Margeat, E., Dosset, P., Arduise, C., Le Grimmelc, C., Royer, C.A., Boucheix, C., Rubinstein, E., and Milhiet, P.E. (2008). Single-molecule analysis of CD9 dynamics and partitioning reveals multiple modes of interaction in the tetraspanin web. *J. Cell Biol.* **182**, 765–776.
- Ewers, H., Smith, A.E., Sbalzarini, I.F., Lillie, H., Koumoutsakos, P., and Helenius, A. (2005). Single-particle tracking of murine polyoma virus-like particles on live cells and artificial membranes. *Proc. Natl. Acad. Sci. USA* **102**, 15110–15115.
- Febbraio, M., Hajjar, D.P., and Silverstein, R.L. (2001). CD36: a class B scavenger receptor involved in angiogenesis, atherosclerosis, inflammation, and lipid metabolism. *J. Clin. Invest.* **108**, 785–791.
- Ferrari, R., Manfroi, A.J., and Young, W.R. (2001). Strongly and weakly self-similar diffusion. *Physica D* **154**, 111–137.
- Foster, L.J., De Hoog, C.L., and Mann, M. (2003). Unbiased quantitative proteomics of lipid rafts reveals high specificity for signaling factors. *Proc. Natl. Acad. Sci. USA* **100**, 5813–5818.
- Friedrichson, T., and Kurzchalia, T.V. (1998). Microdomains of GPI-anchored proteins in living cells revealed by crosslinking. *Nature* **394**, 802–805.
- Gambin, Y., Lopez-Esparza, R., Reffay, M., Sieracki, E., Gov, N.S., Genest, M., Hodges, R.S., and Urbach, W. (2006). Lateral mobility of proteins in liquid membranes revisited. *Proc. Natl. Acad. Sci. USA* **103**, 2098–2102.
- Goswami, D., Gowrishankar, K., Bilgrami, S., Ghosh, S., Raghupathy, R., Chadda, R., Vishwakarma, R., Rao, M., and Mayor, S. (2008). Nanoclusters

Figure 7. CD36 Linear Motion Enhances CD36 Function

(A and B) Effect of cytoskeleton perturbations on CD36 clustering as measured by modal analysis of the intensity histogram (A) and the relative change in the probability of labeled CD36 undergoing merging and splitting events (B). Error bars in (B), SEM from 200 bootstrap samples. **, ns: changes associated with $p < 10^{-4}$ and $p > 0.1$, respectively.

(C) CD36 density on cell surface, measured by immunofluorescence at saturating antibody concentrations. Data from three experiments with 6–12 data points each. Box plots show median (central mark), 25th and 75th percentiles (lower and upper box edges), extent of inlier data points (whiskers) and outliers (blue crosses). *p values < 0.05 in both the Wilcoxon rank-sum test comparing medians and the Kolmogorov-Smirnov test comparing distributions.

(D and E) As in (A) and (B) but calculated from a density-normalized subset of cells. See (A) and (B) for details.

(F) Dil-labeled oxLDL trajectories 5 min after addition to a macrophage, from a 10 Hz/5 s movie before acid wash and a 10 Hz/5 s movie after acid wash. Trajectory color coding and arrows as in Figure 2A. Scale bar, 3 μ m.

(G) Probability of oxLDL undergoing linear motion before and after acid washing (from 994 (before) and 484 (after) trajectories in six cells). Error bars, SEM from 200 bootstrap samples. **p $< 10^{-4}$.

(H) Ratio of phospho-cJun intensity in nucleus to cytoplasm measured by immunofluorescence. Higher ratios indicate more JNK activation. Data from three experiments with ten data points each. See (C) for box plot description. *, ns: $p < 0.05$ and $p > 0.05$, respectively, in both rank-sum and Kolmogorov-Smirnov tests.

(I) oxLDL uptake. Data from three experiments with 5–30 data points each. Box plots and *, as in (C).

(J) Transferrin uptake. Data points from three to five experiments with 5–33 data points each. Box plots and ns, as in (H).

See also Figure S6 and Table S1.

- of GPI-anchored proteins are formed by cortical actin-driven activity. *Cell* 135, 1085–1097.
- Groves, J.T., and Kuriyan, J. (2010). Molecular mechanisms in signal transduction at the membrane. *Nat. Struct. Mol. Biol.* 17, 659–665.
- Harder, T., Kellner, R., Parton, R.G., and Gruenberg, J. (1997). Specific release of membrane-bound annexin II and cortical cytoskeletal elements by sequestration of membrane cholesterol. *Mol. Biol. Cell* 8, 533–545.
- Heldin, C.H. (1995). Dimerization of cell surface receptors in signal transduction. *Cell* 80, 213–223.
- Hess, S.T., Gould, T.J., Gudheti, M.V., Maas, S.A., Mills, K.D., and Zimmerberg, J. (2007). Dynamic clustered distribution of hemagglutinin resolved at 40 nm in living cell membranes discriminates between raft theories. *Proc. Natl. Acad. Sci. USA* 104, 17370–17375.
- Huet, S., Karatekin, E., Tran, V.S., Fanget, I., Cribier, S., and Henry, J.P. (2006). Analysis of transient behavior in complex trajectories: application to secretory vesicle dynamics. *Biophys. J.* 91, 3542–3559.
- Iino, R., Koyama, I., and Kusumi, A. (2001). Single molecule imaging of green fluorescent proteins in living cells: E-cadherin forms oligomers on the free cell surface. *Biophys. J.* 80, 2667–2677.
- Jaqaman, K., Loerke, D., Mettlen, M., Kuwata, H., Grinstein, S., Schmid, S.L., and Danuser, G. (2008). Robust single-particle tracking in live-cell time-lapse sequences. *Nat. Methods* 5, 695–702.
- Kaizuka, Y., Douglass, A.D., Vardhana, S., Dustin, M.L., and Vale, R.D. (2009). The coreceptor CD2 uses plasma membrane microdomains to transduce signals in T cells. *J. Cell Biol.* 185, 521–534.
- Kasai, R.S., Suzuki, K.G.N., Prossnitz, E.R., Koyama-Honda, I., Nakada, C., Fujiwara, T.K., and Kusumi, A. (2011). Full characterization of GPCR monomer-dimer dynamic equilibrium by single molecule imaging. *J. Cell Biol.* 192, 463–480.
- Kennedy, D.J., Kuchibhotla, S., Westfall, K.M., Silverstein, R.L., Morton, R.E., and Febbraio, M. (2011). A CD36-dependent pathway enhances macrophage and adipose tissue inflammation and impairs insulin signalling. *Cardiovasc. Res.* 89, 604–613.
- Kilsdonk, E.P.C., Yancey, P.G., Stoudt, G.W., Bangerter, F.W., Johnson, W.J., Phillips, M.C., and Rothblat, G.H. (1995). Cellular cholesterol efflux mediated by cyclodextrins. *J. Biol. Chem.* 270, 17250–17256.
- Kusumi, A., Ike, H., Nakada, C., Murase, K., and Fujiwara, T. (2005a). Single-molecule tracking of membrane molecules: plasma membrane compartmentalization and dynamic assembly of raft-philic signaling molecules. *Semin. Immunol.* 17, 3–21.
- Kusumi, A., Nakada, C., Ritchie, K., Murase, K., Suzuki, K., Murakoshi, H., Kasai, R.S., Kondo, J., and Fujiwara, T. (2005b). Paradigm shift of the plasma membrane concept from the two-dimensional continuum fluid to the partitioned fluid: high-speed single-molecule tracking of membrane molecules. *Annu. Rev. Biophys. Biomol. Struct.* 34, 351–378.
- Livnah, O., Stura, E.A., Middleton, S.A., Johnson, D.L., Jolliffe, L.K., and Wilson, I.A. (1999). Crystallographic evidence for preformed dimers of erythropoietin receptor before ligand activation. *Science* 283, 987–990.
- Long, B.R., and Vu, T.Q. (2010). Spatial structure and diffusive dynamics from single-particle trajectories using spline analysis. *Biophys. J.* 98, 1712–1721.
- Manneville, J.B., Etienne-Manneville, S., Skehel, P., Carter, T., Ogden, D., and Ferenczi, M. (2003). Interaction of the actin cytoskeleton with microtubules regulates secretory organelle movement near the plasma membrane in human endothelial cells. *J. Cell Sci.* 116, 3927–3938.
- McGilvray, I.D., Serghides, L., Kapus, A., Rotstein, O.D., and Kain, K.C. (2000). Nonopsonic monocyte/macrophage phagocytosis of *Plasmodium falciparum*-parasitized erythrocytes: a role for CD36 in malarial clearance. *Blood* 96, 3231–3240.
- McGrath, J.L., Tardy, Y., Dewey, C.F., Jr., Meister, J.J., and Hartwig, J.H. (1998). Simultaneous measurements of actin filament turnover, filament fraction, and monomer diffusion in endothelial cells. *Biophys. J.* 75, 2070–2078.
- Ohtani, Y., Irie, T., Uekama, K., Fukunaga, K., and Pitha, J. (1989). Differential effects of alpha-cyclodextrins, beta-cyclodextrins and gamma-cyclodextrins on human erythrocytes. *Eur. J. Biochem.* 186, 17–22.
- Pike, L.J. (2003). Lipid rafts: bringing order to chaos. *J. Lipid Res.* 44, 655–667.
- Plowman, S.J., Muncke, C., Parton, R.G., and Hancock, J.F. (2005). H-ras, K-ras, and inner plasma membrane raft proteins operate in nanoclusters with differential dependence on the actin cytoskeleton. *Proc. Natl. Acad. Sci. USA* 102, 15500–15505.
- Ponti, A., Matov, A., Adams, M., Gupton, S., Waterman-Storer, C.M., and Danuser, G. (2005). Periodic patterns of actin turnover in lamellipodia and lamellae of migrating epithelial cells analyzed by quantitative Fluorescent Speckle Microscopy. *Biophys. J.* 89, 3456–3469.
- Rahaman, S.O., Lennon, D.J., Febbraio, M., Podrez, E.A., Hazen, S.L., and Silverstein, R.L. (2006). A CD36-dependent signaling cascade is necessary for macrophage foam cell formation. *Cell Metab.* 4, 211–221.
- Rodriguez, O.C., Schaefer, A.W., Mandato, C.A., Forscher, P., Bement, W.M., and Waterman-Storer, C.M. (2003). Conserved microtubule-actin interactions in cell movement and morphogenesis. *Nat. Cell Biol.* 5, 599–609.
- Sako, Y., Minoghchi, S., and Yanagida, T. (2000). Single-molecule imaging of EGFR signalling on the surface of living cells. *Nat. Cell Biol.* 2, 168–172.
- Savill, J. (1997). Recognition and phagocytosis of cells undergoing apoptosis. *Br. Med. Bull.* 53, 491–508.
- Saxton, M.J., and Jacobson, K. (1997). Single-particle tracking: applications to membrane dynamics. *Annu. Rev. Biophys. Biomol. Struct.* 26, 373–399.
- Schamel, W.W.A., Arechaga, I., Risueño, R.M., van Santen, H.M., Cabezas, P., Risco, C., Valpuesta, J.M., and Alarcón, B. (2005). Coexistence of multivalent and monovalent TCRs explains high sensitivity and wide range of response. *J. Exp. Med.* 202, 493–503.
- Scott, J.D., and Pawson, T. (2009). Cell signaling in space and time: where proteins come together and when they're apart. *Science* 326, 1220–1224.
- Serge, A., Furgeaud, L., Hemar, A., and Choquet, D. (2003). Active surface transport of metabotropic glutamate receptors through binding to microtubules and actin flow. *J. Cell Sci.* 116, 5015–5022.
- Sethna, J.P. (2006). *Statistical mechanics: entropy, order parameters and complexity* (New York: Oxford University Press).
- Sharma, P., Varma, R., Sarasij, R.C., Ira, Gousset, K., Krishnamoorthy, G., Rao, M., and Mayor, S. (2004). Nanoscale organization of multiple GPI-anchored proteins in living cell membranes. *Cell* 116, 577–589.
- Subbaramaiah, K., Hart, J.C., Norton, L., and Dannenberg, A.J. (2000). Microtubule-interfering agents stimulate the transcription of cyclooxygenase-2. Evidence for involvement of ERK1/2 AND p38 mitogen-activated protein kinase pathways. *J. Biol. Chem.* 275, 14838–14845.
- Suzuki, K.G.N., Fujiwara, T.K., Sanematsu, F., Iino, R., Edidin, M., and Kusumi, A. (2007). GPI-anchored receptor clusters transiently recruit Lyn and G alpha for temporary cluster immobilization and Lyn activation: single-molecule tracking study 1. *J. Cell Biol.* 177, 717–730.
- Thorne, R.F., Marshall, J.F., Shafren, D.R., Gibson, P.G., Hart, I.R., and Burns, G.F. (2000). The integrins alpha3beta1 and alpha6beta1 physically and functionally associate with CD36 in human melanoma cells. Requirement for the extracellular domain OF CD36. *J. Biol. Chem.* 275, 35264–35275.
- Varma, R., and Mayor, S. (1998). GPI-anchored proteins are organized in submicron domains at the cell surface. *Nature* 394, 798–801.
- Viola, A., and Gupta, N. (2007). Tether and trap: regulation of membrane-raft dynamics by actin-binding proteins. *Nat. Rev. Immunol.* 7, 889–896.
- Yang, G., Houghtaling, B.R., Gaetz, J., Liu, J.Z., Danuser, G., and Kapoor, T.M. (2007). Architectural dynamics of the meiotic spindle revealed by single-fluorophore imaging. *Nat. Cell Biol.* 9, 1233–1242.
- Yujiri, T., Fanger, G.R., Garrington, T.P., Schlesinger, T.K., Gibson, S., and Johnson, G.L. (1999). MEK kinase 1 (MEKK1) transduces c-Jun NH2-terminal kinase activation in response to changes in the microtubule cytoskeleton. *J. Biol. Chem.* 274, 12605–12610.
- Zeng, Y.C., Tao, N.B., Chung, K.N., Heuser, J.E., and Lublin, D.M. (2003). Endocytosis of oxidized low density lipoprotein through scavenger receptor CD36 utilizes a lipid raft pathway that does not require caveolin-1. *J. Biol. Chem.* 278, 45931–45936.

EXTENDED EXPERIMENTAL PROCEDURES

Reagents

Latrunculin B, blebbistatin and nocodazole were purchased from Calbiochem; unlabeled and Dil-labeled oxidized-LDL (oxLDL) from Intracel; and methyl- β -cyclodextrin, filipin and Cy3-conjugated anti- β -tubulin (clone TUB 2.1) from Sigma. Qdot 655-goat F(ab')₂ anti-mouse IgG conjugates, the Amplex Red cholesterol determination assay, the Alexa Fluor-555 conjugates of transferrin and cholera toxin B subunit, and the CellLight Tubulin-GFP BacMam 2.0 system were from Invitrogen. Phospho-c-Jun (Ser63) II antibody was from Cell Signaling.

Fab Labeling Validation

The purity of the anti-CD36 Fab fragment preparations was verified by immunoblotting. Binding of the Fab to the cells was specific, since virtually no secondary Fab was bound to cells preincubated with comparable or even higher concentrations of irrelevant isotype-matched Fab fragments or full antibodies.

At the concentration used for labeling of macrophages, only one Cy3-conjugated secondary Fab fragment was bound per primary Fab. This was deduced from comparing the emission intensity of the complexes detected on cells labeled with the lowest concentration of primary Fab to the step size of the photobleaching of individual fluorescent spots (Figure 1). Moreover, *in vitro* experiments immobilizing anti-CD36 on glass showed that at the concentration of Cy3-conjugated secondary Fab used on macrophages, only one secondary Fab fragment bound per primary.

In a limited number of experiments the primary anti-CD36 Fab was directly labeled with Cy3 using the Cy3mAB labeling kit from Amersham. The results of these experiments, where the secondary antibody was obviated, were similar to those using indirect immunolabeling. Given this confirmation, all experiments used for this study were conducted using the primary plus secondary indirect labeling strategy, which offered more flexibility for titration and permitted the use of commercially available labeled secondary Fab.

The CD36 clusters detected on the cells were inherent features of the cells and not the result of antibody-induced crosslinking or of multiple secondary Fab fragments binding on single primary Fab fragments. Several lines of evidence support this contention. First, the clusters were observed when the cells were fixed before exposure to the Fab fragments. Second, the more intensely fluorescent complexes were obtained when increasing the concentration of the unlabeled primary Fab while keeping the concentration of Cy3-conjugated secondary Fab constant. Under these conditions, the number of secondary Fab fragments per primary did not increase and, in fact, was more likely to decrease as additional primary Fab molecules bound to the cells. Lastly, we found no evidence of crosslinking or activation of CD36 when exposed to Fab fragments. While in live cells the receptors readily internalize upon crosslinking, they remained on the cell surface following exposure to the primary and secondary Fab fragments. This was verified by optical slicing using spinning disk microscopy, by acid washing (Figures S2C–S2H), and by assessing exposure of the complexes to a tertiary antibody.

Quantum Dot Labeling Validation

At the concentrations used, no significant binding of Qdots to the cells was observed when the primary anti-CD36 antibody was omitted or when using an irrelevant isotype-matched primary antibody. This finding ruled out nonspecific engagement of Fc γ receptors, which are known to have very low affinity for monomeric IgG. For some of the experiments we were unable to use primary Fab fragments, because the F(ab')₂ anti-mouse IgG coupled to the Qdots used in the early stages of this study failed to recognize Fab fragments. However, by preventing crosslinking, we obtained a general receptor distribution and motion pattern that was very similar to that obtained with Fab fragments.

Quantification of Cytoskeleton-Associated CD36

The association of CD36 with the cytoskeleton was estimated by extraction with nonionic detergents. Because the supply of primary human macrophages is limited, these experiments were performed using the human monocyte/macrophage U937 line (ATCC) differentiated for 2 days using phorbol myristate acetate. CD36 was tagged in cells grown on 10 cm culture dishes after blocking with 4% donkey serum in HBSS for 30 min by incubation with mouse anti-CD36 (1:1000) for 20 min, followed by washing and incubation with horseradish peroxidase-conjugated donkey anti-mouse antibody (1:1000), also for 20 min. After washing, the cells were extracted with either 0.1% or 1% Triton X-100 in PBS for 5 min. All the preceding steps were performed at 4°C, to minimize crosslinking, internalization and/or proteolysis. Where indicated, the cells were treated for 20 min with 10 μ M latrunculin B prior to extraction. That Triton X-100 fully lysed the cells under all conditions tested was confirmed by quantifying the solubilization of GAPDH by Western blotting.

To quantify the amount of antibody associated with the intact or extracted cells, peroxidase activity was detected by incubating cells with 0.4 mg/ml *o*-phenylenediamine dihydrochloride (Sigma FAST-OPD) according to the manufacturer's instructions. Reactions were stopped after 15 min with 3 M HCl, and absorbance at 492 nm was determined with a spectrophotometer. Background readings, obtained by omitting the primary antibody, were determined separately for each condition and subtracted from the total absorbance.

Measurement of Cholesterol Depletion by Methyl- β -Cyclodextrin

Where indicated, cholesterol was extracted by incubating the cells with 10 mM methyl- β -cyclodextrin (M β CD) for 30 min at 37°C. Two independent methods were used to quantify the cholesterol content of macrophages before and after the extraction. Unesterified cholesterol was measured fluorimetrically using the Amplex® Red Cholesterol Assay Kit from Invitrogen, as described by the manufacturers. Unesterified cholesterol was also measured by epifluorescence microscopy after fixing cells in 4% paraformaldehyde, followed by quenching with 100 mM glycine and staining for 16 hr at 4°C with 0.5 mg/ml filipin. Following background subtraction, the fluorescence of individual cells (excitation 350/50 nm, emission 460/50 nm) was integrated.

Diffusion Analysis and Classification of CD36 Motion in the Membrane

Multiple-particle tracking of CD36 in unstimulated macrophages indicated that the receptors exhibited several trajectory types (Figure 2A). To identify and characterize the different trajectory types, we analyzed individual trajectories using two measures: (i) trajectory shape and (ii) diffusion analysis.

Trajectory Shape

The first measure classified trajectory shape based on the degree of anisotropy of the scatter of particle positions along a trajectory (Huet et al., 2006), as described in detail in (Jaqaman et al., 2008). This measure characterized the shape of a trajectory regardless of the nature of the underlying particle motion. With this, trajectories with a high degree of anisotropy were classified as ‘linear’, while the others were considered ‘isotropic’.

Diffusion Analysis

Diffusion type classification and diffusion coefficient estimation. The second measure extracted diffusion types using a moment scaling spectrum (MSS) analysis of particle displacements (Ewers et al., 2005; Ferrari et al., 2001). This analysis was applied to full 2D displacements, and to 1D displacements in linear trajectories as obtained by decomposing each displacement into its components parallel and perpendicular to the orientation axis (Figure 3A). In brief, the MSS analysis consisted of the following steps for each trajectory:

(1) For each time shift τ , the 0th to 6th displacement moments, $\mu_0(\tau)$ to $\mu_6(\tau)$, were calculated (note that the commonly used mean square displacement (MSD) is the second moment).

(2) From the relationships $\mu_m(\tau) = 4D_m\tau^{\alpha_m}$ for 2D analysis and $\mu_m(\tau) = 2D_m\tau^{\alpha_m}$ for 1D analysis for $m = 0 \dots 6$, describing how each moment scaled with time shift τ , the generalized diffusion coefficient D_m and power α_m were estimated. (In the commonly used MSD analysis, the power $\alpha_2 = 1$ for unconfined diffusion). The second moment yielded the “normal” diffusion coefficient D_2 .

(3) The plot of α_m versus m is called the moment scaling spectrum. For a strongly self-similar process, it follows a straight line, the slope of which indicates the type of motion underlying the analyzed trajectory: A slope of 0.5 implies normal diffusion, a slope < 0.5 indicates sub-diffusion, and a slope > 0.5 indicates super-diffusion.

Because of the finite length of CD36 trajectories, however, we could not use 0.5 as the cutoff between the different motion types. Instead, we estimated trajectory length-dependent sub-diffusion and super-diffusion cutoffs that ensured 95% confidence in the classification. We obtained the cutoffs for trajectories of length 20–500 frames; trajectories shorter than 20 frames were too short to analyze and classify, while for trajectories longer than 500 frames (which was achieved only by Qdot labeling) the cutoffs were approximated by the value at 500 frames. To determine the cutoffs as functions of trajectory length, we generated 30000 1D and 30000 2D Brownian trajectories at every length and subjected them to the MSS analysis, thus obtaining a distribution of MSS line slopes at every length (Figure S2A shows the distribution in the 2D case). For each dimension, the length-dependent confined-diffusion cutoffs were then taken as the 5th percentile of the distributions, while the super-diffusion cutoffs were taken as the 95th percentile of the distributions. We verified that these thresholds were independent of the Brownian motion diffusion coefficient by performing two separate simulations with different diffusion coefficients (1 and 0.1 pixels²/unit time).

Confinement Dimension Estimation. For confined trajectories and linear trajectories, we also calculated their confinement dimensions. For comparability, we approximated both confinement regions by rectangles. In the case of a linear trajectory, the short edge of the rectangle corresponded to its width perpendicular to the orientation axis (Figure 3A). In the case of an isotropically confined trajectory, both edges were approximately equal, since, by definition, positional variation was almost uniform in all directions. Thus the rectangle effectively reduced to a square, and we approximated the confinement dimensionality by the average rectangle edge length.

The rectangle edge lengths were derived via eigenvalue decomposition of the variance-covariance matrix of particle positions along each trajectory. The long rectangle edge was taken to be parallel to the eigenvector corresponding to the larger eigenvalue λ_l , and its length L_l was approximated by $L_l = \sqrt{3\lambda_l}$. Similarly, the short rectangle edge was taken to be parallel to the eigenvector corresponding to the smaller eigenvalue λ_s , and its length L_s was approximated by $L_s = \sqrt{3\lambda_s}$. The equation $L_{l,s} = \sqrt{3\lambda_{l,s}}$ was derived by (i) assuming that particle motion inside the confinement region was a random walk, in which case a particle would visit every position inside its confinement region with uniform probability (Dorn et al., 2005), and (ii) considering that the eigenvalues represented the variances of particle positions along the corresponding rectangle edges.

Quantification of Radiality of Linear Trajectories

To quantify the extent of the radial arrangement of linear trajectories around the perinuclear region of a cell, we (i) calculated for each linear trajectory the angle between its orientation axis and the ray connecting the “cell center” to the trajectory center (the angle θ in

Figure S2B), and (ii) averaged θ over all linear trajectories in the cell to obtain the average angle $\bar{\theta}$. For a perfectly radial arrangement, $\bar{\theta} = 0$. For randomly oriented linear trajectories, the distribution of θ was expected to be uniform between 0° and 90° and thus $\bar{\theta} = 45^\circ$. In practice, even though we knew where the nucleus was, we did not know the exact location of the “cell center.” Therefore, we solved an optimization problem where the cell center was taken as that point in space which minimized $\bar{\theta}$. With this, we determined both the location of the “cell center” and $\bar{\theta}$, thus quantifying the extent of the radial arrangement of linear trajectories.

Because of the optimization approach, $\bar{\theta}$ for randomly oriented linear trajectories was now expected to be slightly smaller than 45° . By performing the optimization and estimating $\bar{\theta}$ from 20 sets of simulated, randomly oriented trajectories (with 200 trajectories per set), we found that $\bar{\theta} = 42^\circ \pm 0.3^\circ$. This value was compared to $\bar{\theta}$ of CD36 (Figure 2C), CTB (Figure 4C) and Fc γ receptor (Figure S4D).

Simulation of Apparent Receptor Fusion Times due to Resolution Limitations

In order to estimate our confidence in the observed clustering of linearly moving receptors, we simulated receptors undergoing 1D diffusion with a diffusion coefficient = $0.1 \mu\text{m}^2/\text{s}$, as observed for linearly moving CD36 (Figure 3H). At the start of the simulation, the two receptors were separated by the practical resolution limit, estimated to be approximately 300 nm from (i) fitting point spread function models (i.e., Gaussians with unknown width) to isolated single receptor images in live cells and (ii) approximating the Rayleigh resolution limit as three-times the fitted Gaussian standard deviation. In about half of the simulations, the receptors happened to approach each other in the second frame, resulting in an apparent fusion of their particle images. We then measured the time interval until the particle images split, i.e., until the distance between the receptors became again larger than 300 nm, assuming that while apparently fused the particles diffused without interacting with each other. By repeating this analysis 5000 times we calculated our confidence that the experimentally observed transient fusions of linearly moving receptors represented events of genuine clustering between receptors as opposed to incidental particle image fusions (Figure 2G). As expected, the confidence in a fusion representing receptor interactions increased with its duration. 60% of the experimentally observed fusion durations were > 1 s, the 90% confidence level derived from simulations. Of note, none of the apparent fusions in the simulation lasted for more than 3.6 s, while 16% of the experimental fusion durations were > 3.6 s.

We performed similar simulations to estimate our confidence in the transient fusions of isotropic-unconfined receptors. In these simulations, the receptors underwent 2D diffusion with a diffusion coefficient = $0.06 \mu\text{m}^2/\text{s}$, as observed for isotropic-unconfined CD36 (Figure 3H). Because of the increased freedom of movement in 2D compared to 1D, the distribution of apparent fusion times obtained from these simulations was shifted toward smaller values compared to the distribution resulting from 1D diffusion. Thus, in the case of randomly moving receptors, the 90% confidence level was at 0.8 s. In agreement with the linear case, 57% of the experimentally observed fusion durations for randomly moving receptors were > 0.8 s (data not shown).

Estimation of CD36 Surface Density

We estimated two types of CD36 surface densities from single molecule images:

Overall Density

We counted the number of receptors in images of fixed cells with the highest, receptor-saturating labeling density (1:300 primary Fab dilution), and divided that number by the estimated cell area. The number of receptors in an image was counted by first detecting the fluorescent particles and then using particle intensity to estimate the number of receptors making up each particle. The intensity of a single Cy3 fluorophore labeling a single CD36 was taken as 0.06 units, as derived from the modal analysis of intensity histograms and from the step photobleaching of individual particles (Figure 1). Thus a particle with intensity $< 1.5 \times 0.06$ units most probably represented a single receptor, a particle with intensity $> 1.5 \times 0.06$ and $< 2.5 \times 0.06$ units most probably represented two receptors, etc. With this, the overall CD36 density was estimated to be 1.5 receptors/ μm^2 .

Effective Density Based on Motion Type

The effective surface density of receptors, which regulates their ability to encounter each other and cluster, depends on the size and shape of the area in which they are able to freely diffuse. The above calculation ignores these factors and assumes that receptors can freely diffuse throughout the whole cell surface. Thus, it is applicable to freely diffusing receptors. However, for linearly moving receptors where motility is restricted along one dimension, the above calculated overall density of receptors deviates from, and is expected to be lower than, the effective receptor density in regions with confined diffusion.

To calculate effective densities based on motion type, we used live-cell movies that allowed us to classify receptors as linearly moving versus isotropically moving (both free and confined). Because receptors with the different motion types intermingled in space, it was difficult to estimate effective densities by determining areas of linear motion and areas of isotropic motion on the cell surface and counting receptors in each area. Instead, we used nearest neighbor distances per motion category as a means to estimating receptor densities. Specifically,

(1) we calculated the average nearest neighbor distances nnd_{random} and nnd_{linear} for receptors undergoing isotropic and linear motion, respectively;

(2) we estimated $area_{\text{random}} = \pi \times (nnd_{\text{random}})^2$ and $area_{\text{linear}} = 2 \times nnd_{\text{linear}} \times 0.2$ as the areas where on average 2 receptors are found for isotropically moving and linearly moving receptors, respectively (defining the width of linear confinement areas as $0.2 \mu\text{m}$);

(3) we calculated the effective density for isotropically and linearly moving receptors as $2 / area_{\text{random}}$ and $2 / area_{\text{linear}}$, respectively.

Applying this analysis to 16 unperturbed live cells, the average nearest neighbor distance for isotropically and linearly moving receptors was found to be 1.0 and 1.2 μm , respectively. With this, the effective receptor density for linearly moving receptors was five to ten times larger than the effective receptor density for isotropically moving receptors.

While the live-cell movies allowed us to classify receptors as isotropically moving or linearly moving, their receptor labeling was unsaturated and thus they underestimated the effective densities. To get better estimates of the effective densities, we should apply this analysis to fixed cells, where labeling density was highest (1:300 dilution of primary fab fragments). However, in fixed cells, we did not know which particle underwent which motion type. To resolve these conflicting requirements, we made use of the fact that, in live cells, the nearest neighbor distances were similar for the two motion categories. Thus, we calculated the average nearest neighbor distance in fixed cells, found to be 0.6 μm , and used that value for both nnd_{random} and nnd_{linear} , from which we calculated $area_{\text{random}}$ and $area_{\text{linear}}$ and then the effective densities. This yielded effective densities of 1.7 and 8.2 receptors / μm^2 for isotropically moving and linearly moving receptors.

Two results followed from this calculation: first, the two approaches for calculating receptor density ((1) counting receptors and dividing by area and (2) using the nearest neighbor distance) yielded similar results when applied to the same dataset and under the assumption of free diffusion (which is inherent to the first approach). Second, even though the absolute effective densities were underestimated in live cells, the ratio of effective densities is maintained. In conclusion, the motion of receptors within linear confinement regions increased the effective receptor density by approximately five times.

SUPPLEMENTAL REFERENCES

- Dorn, J.F., Jaqaman, K., Rines, D.R., Jelson, G.S., Sorger, P.K., and Danuser, G. (2005). Yeast kinetochore microtubule dynamics analyzed by high-resolution three-dimensional microscopy. *Biophys. J.* *89*, 2835–2854.
- Ewers, H., Smith, A.E., Sbalzarini, I.F., Lilie, H., Koumoutsakos, P., and Helenius, A. (2005). Single-particle tracking of murine polyoma virus-like particles on live cells and artificial membranes. *Proc. Natl. Acad. Sci. USA* *102*, 15110–15115.
- Ferrari, R., Manfroi, A.J., and Young, W.R. (2001). Strongly and weakly self-similar diffusion. *Physica D* *154*, 111–137.
- Huet, S., Karatekin, E., Tran, V.S., Fanget, I., Cribier, S., and Henry, J.P. (2006). Analysis of transient behavior in complex trajectories: application to secretory vesicle dynamics. *Biophys. J.* *91*, 3542–3559.
- Jaqaman, K., Loerke, D., Mettlen, M., Kuwata, H., Grinstein, S., Schmid, S.L., and Danuser, G. (2008). Robust single particle tracking in live-cell time-lapse sequences. *Nat. Methods* *5*, 695–702.
- Koller, T., Gerig, G., Szekely, G., and Dettwiler, D. (1995). Multiscale Detection of Curvilinear structure in 2-D and 3-D Image Data. Paper presented at: Fifth International Conference on Computer Vision ICCV'95 (Cambridge, MA: IEEE Computer Society Press).

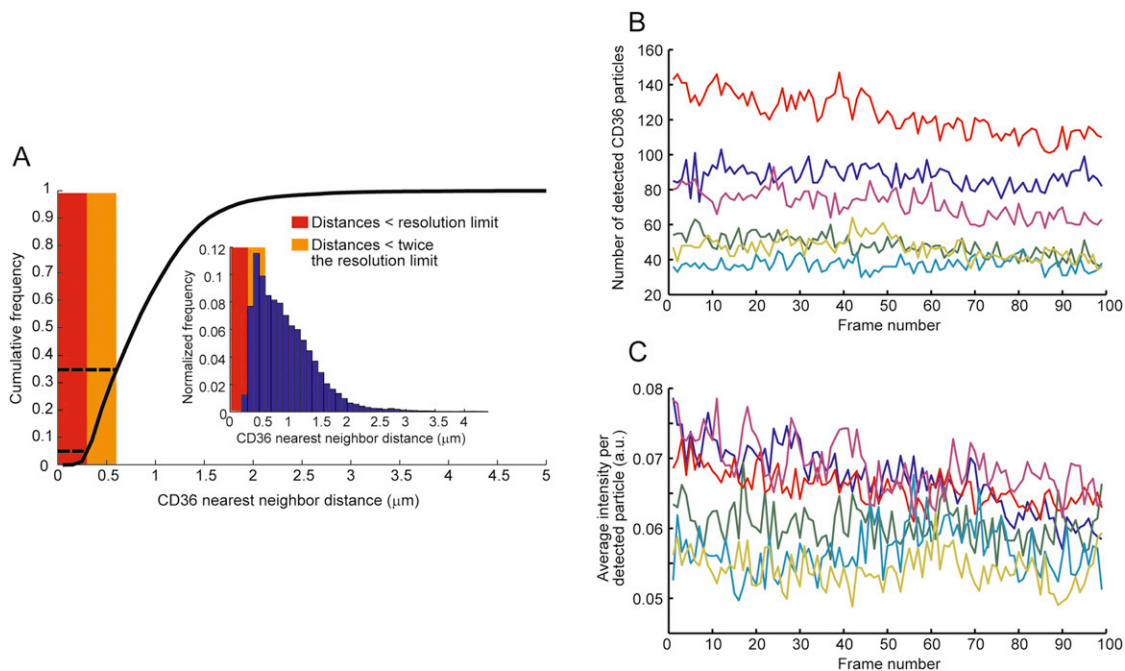


Figure S1. Single-Molecule Imaging of CD36 in Primary Human Macrophages, Related to Figure 1

(A) Cumulative frequency of receptor nearest neighbor distances at 1:3000 dilution of primary Fab fragments. Inset: Normalized frequency of receptor nearest neighbor distances. Gaussian mixture model fitting allowed the measurement of receptor positions when receptor images overlapped (red and orange areas; $\sim 35\%$ of receptors) and when inter-receptor distances were below the diffraction-limited optical resolution (red area; $\sim 5\%$ of detected receptors). The diffraction-limited optical resolution was estimated to be ~ 300 nm from (i) fitting point spread function models (i.e., Gaussians with unknown width) to isolated single receptor images in live cells and (ii) approximating the Rayleigh resolution limit as three-times the fitted Gaussian standard deviation.

(B and C) Cy3 photobleaching in the 10 s of live-cell imaging was negligible, as indicated by the constant number of particles (B) and constant average particle intensity (C) throughout each of the 6 movies of unperturbed macrophages.

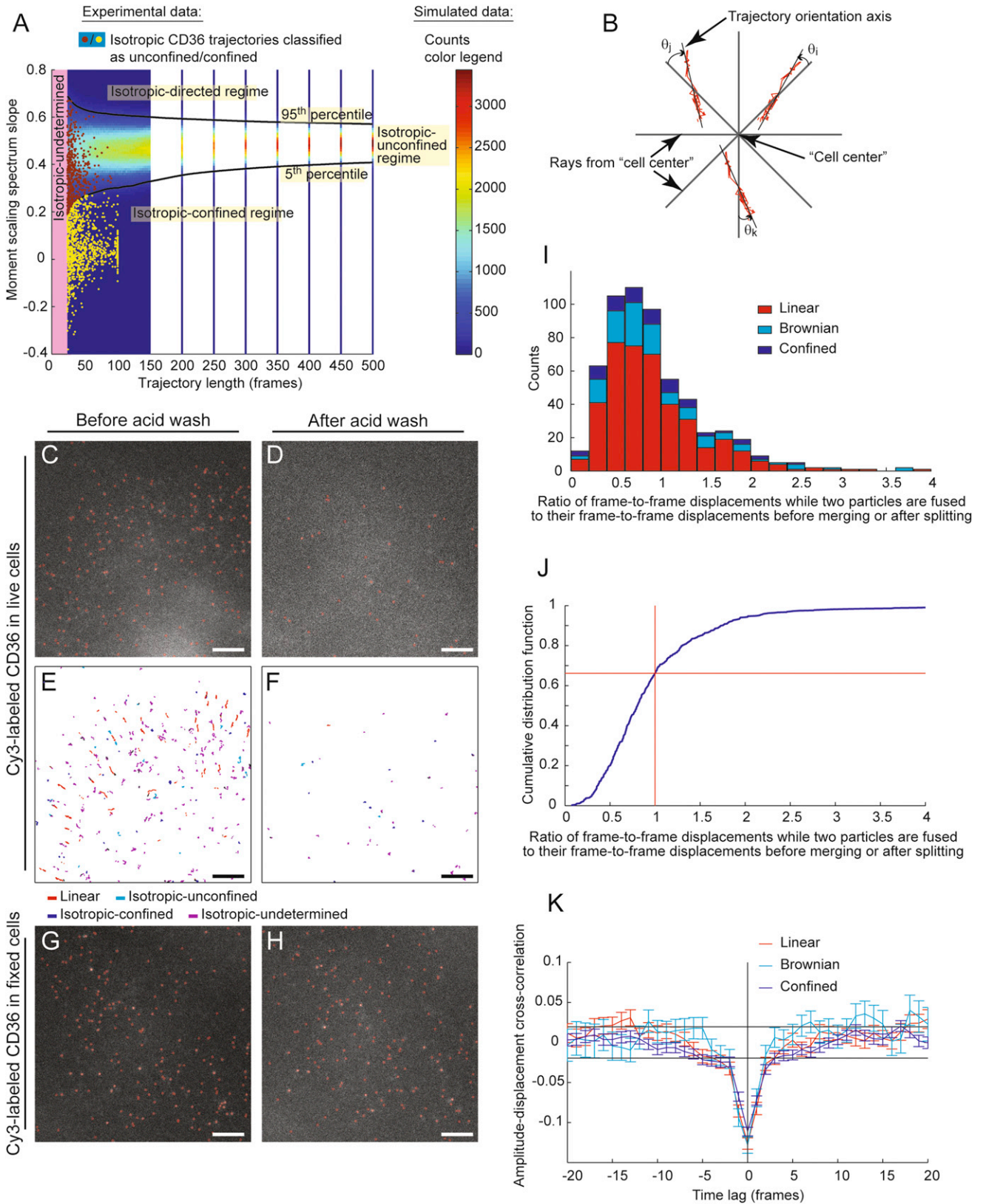


Figure S2. A Subpopulation of CD36 Moves along Linear Trajectories that Enhance Receptor Clustering, Related to Figure 2

(A) MSS slope thresholds derived from 30,000 simulations to classify the diffusion types of isotropic trajectories. Color bar shows number of simulations falling in the different histogram bins for each trajectory length. Brown and yellow dots show the MSS slopes obtained for the experimental data.

(B) Illustration of the angle θ quantifying the deviation of linear trajectories from perfect radiality. Shown are three sample trajectories (i, j, k).

(C–H) Acid wash control showing that recorded CD36 motion was on the cell surface.

(C and D) Live-cell image and detection results before (C) and after (D) acid washing. Only 15% of fluorescence remained after acid wash. Scale bar (in all panels), 5 μm .

(E and F) CD36 trajectories in a 10 Hz/20 frame live-cell movie before (E) and after (F) acid wash. None of the remaining receptors (15% of original) exhibited linear motion after acid wash.

(G and H) Image and detection results before (G) and after (H) acid washing a cell fixed with 8% paraformaldehyde. After fixation, 85% of the fluorescence remained after acid wash, indicating that the loss of fluorescence from live cells was not due to effects of the acid medium on Cy3 fluorescence, but was due to the release of Cy3-Fab fragments bound to CD36 residing in the plasma membrane.

(I–K) Relationship between CD36 mobility and clustering.

(I) Histogram showing ratio of frame-to-frame displacements of fused receptors to their displacements before merging or after splitting for the different motion types. Before/after frame-to-frame displacements were calculated by taking the average displacements from three time points before/after each merging or splitting event.

(J) Cumulative distribution of the ratios shown in (I) for all motion types together. 65% of the ratios are below one, indicating that receptor mobility went down in 65% of the cases while receptors were fused.

(K) Cross-correlation between particle intensity and frame-to-frame displacement, providing further evidence that receptor mobility tended to go down as particle intensity went up.

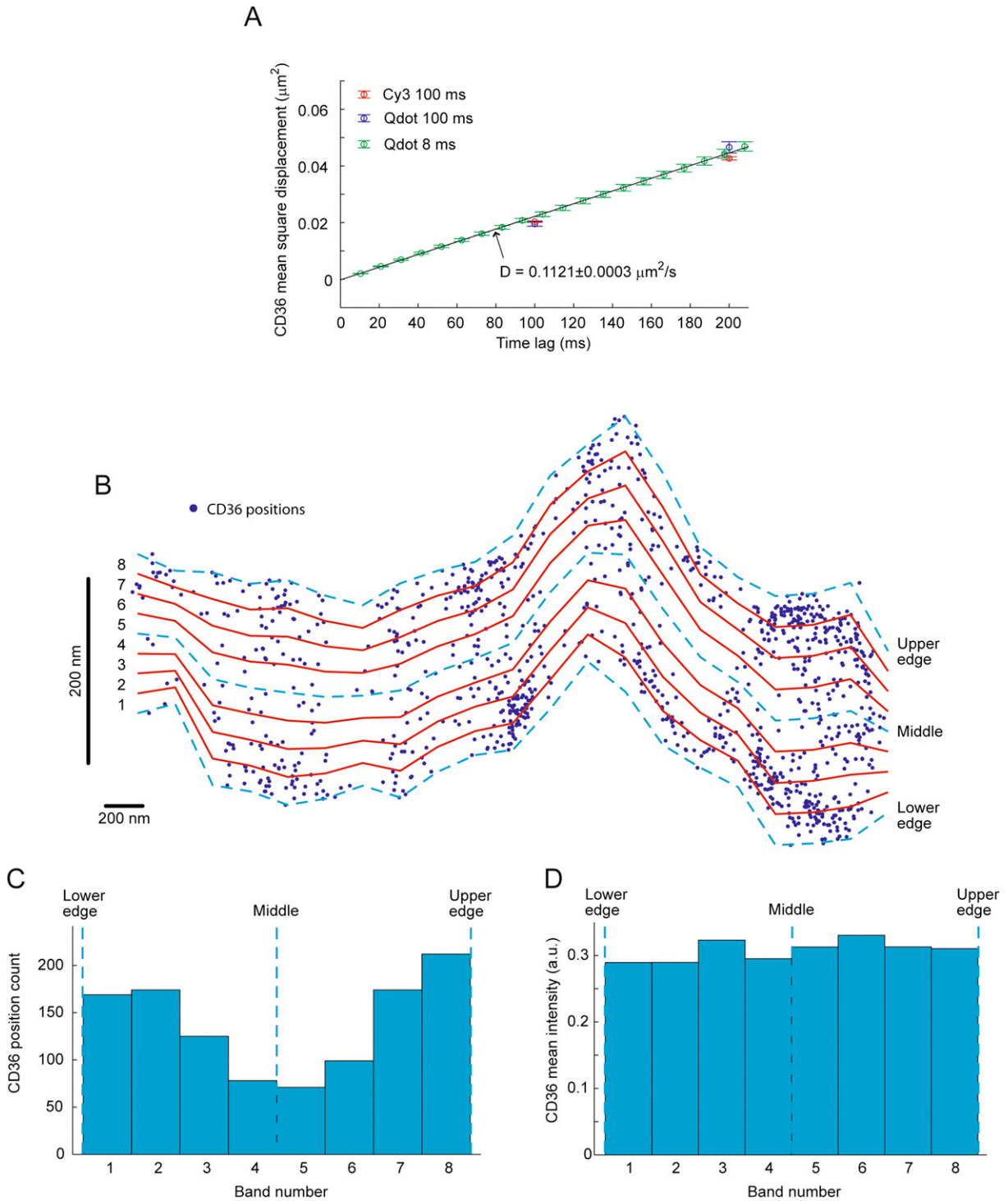


Figure S3. CD36 Linear Motion Is Diffusion within Linear Confinement Regions, Related to Figure 3

(A) Mean square displacement (MSD) of CD36 along the orientation axis of linear trajectories, derived from 125 Hz Qdot movies. Error bars, SEM from > 1000 data points per time lag. The straight line relationship between the MSD and time lag indicates 1D freely diffusive motion.

(B–D) Calculation of receptor positional and intensity distribution across a linear trajectory's width.

(B) Division of linear trajectory into eight bands of equal-width that run parallel to its walls. Note the unequal horizontal and vertical dimensions used for illustration.

(C) Number of times the receptor is found in each band (shown also in Figure 3E).

(D) Average particle intensity in each band. Note that, while the receptors showed a preference for the edges (C), the intensity of the receptors was uniform across the width of the linear confinement regions. This excluded the possible interpretation of the position histogram as representing movement on the surface of three dimensional “tubes” or “ruffles,” in which case two dimensional imaging that ignored the z-coordinate would also result in a position histogram similar to that observed in (C).

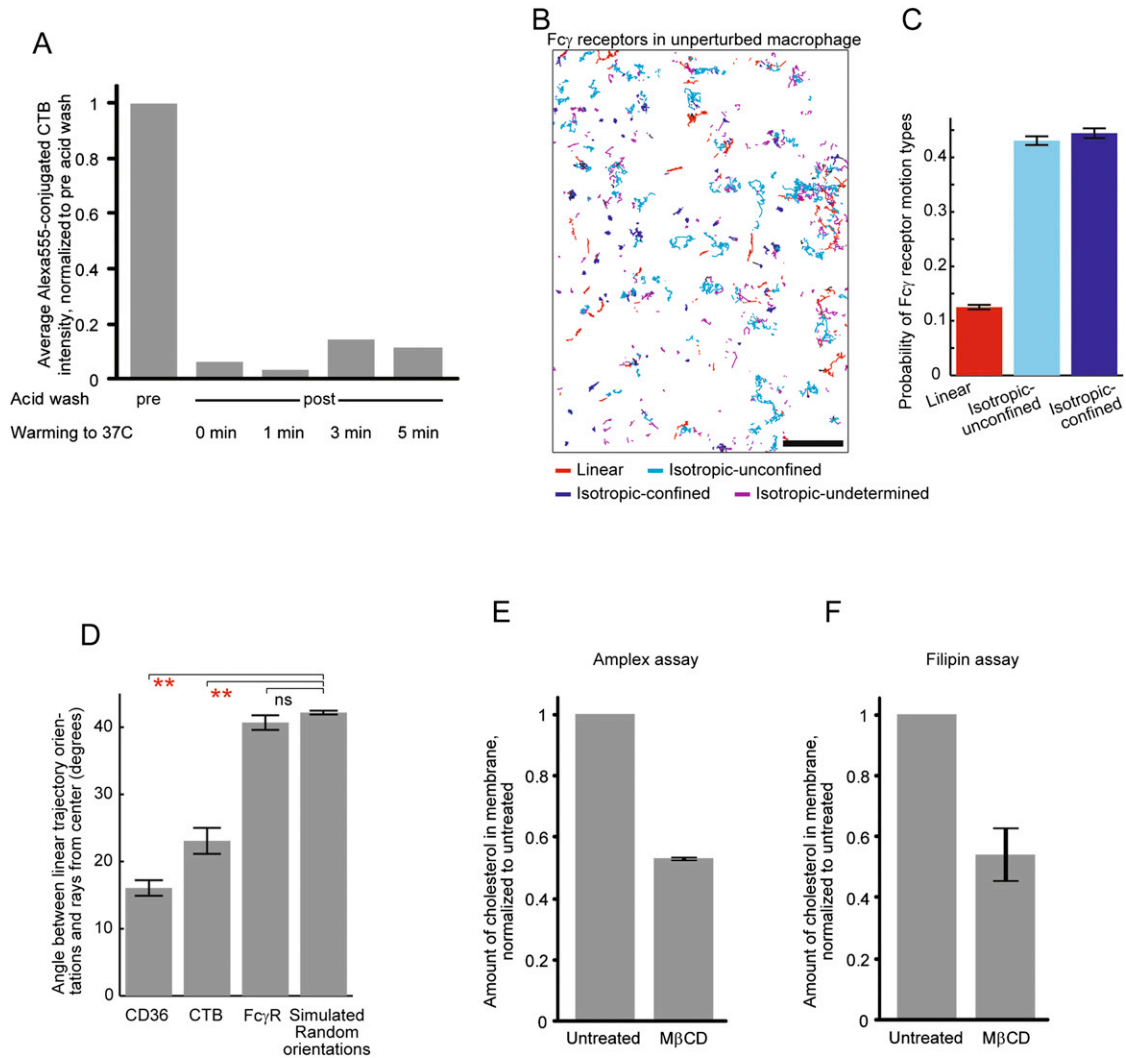


Figure S4. CD36 Linear Motion Does Not Depend on Rafts, Related to Figure 4

(A) Acid washing removed the majority of Alexa555-conjugated cholera toxin subunit B (CTB), confirming that the imaged CTB (Figure 4A) was on the cell surface. Data shown are the average of at least 50 cells per condition.

(B) Trajectories of Cy3-immunolabeled Fab fragments of the IV.3 antibody against the Fc γ receptor in a primary human macrophage from a 10 Hz/10 s movie. Scale bar, 5 μ m. Red, linear trajectories; cyan, isotropic-unconfined trajectories; blue, isotropic-confined trajectories; purple, isotropic trajectories too short for MSS analysis and thus have an undetermined diffusion type (i.e., trajectories lasting for at least 5 frames but shorter than 20 frames).

(C) Probability of Fc γ receptors undergoing the different motion types, derived from 13676 trajectories in 10 cells. Error bars, SEM calculated for each condition from 200 bootstrap samples. The fraction of trajectories classified as linear (12%) was marginally above the hypothesis test alpha-value of 0.1.

(D) Mean deviation, in degrees, of the orientation of Fc γ receptors, CD36 and CTB linear trajectories from a perfect radial arrangement about the perinuclear region. Error bars, SEM from 19 cells for CD36, 23 cells for CTB, 10 cells for Fc γ receptors and 20 simulations. In contrast to CD36 and CTB, the deviation of the Fc γ receptor linear trajectories was not significantly different from the deviation of simulated random orientations. Thus, Fc γ receptors did not exhibit radially arranged linear motion.

(E and F) Quantification of cholesterol content in the membrane. Unesterified cholesterol was estimated using cholesterol oxidase and the fluorimetric Amplex Red assay (E) or by staining the cells with filipin and integrating the fluorescence of individual cells (F). Data are means \pm SEM from three independent experiments each.

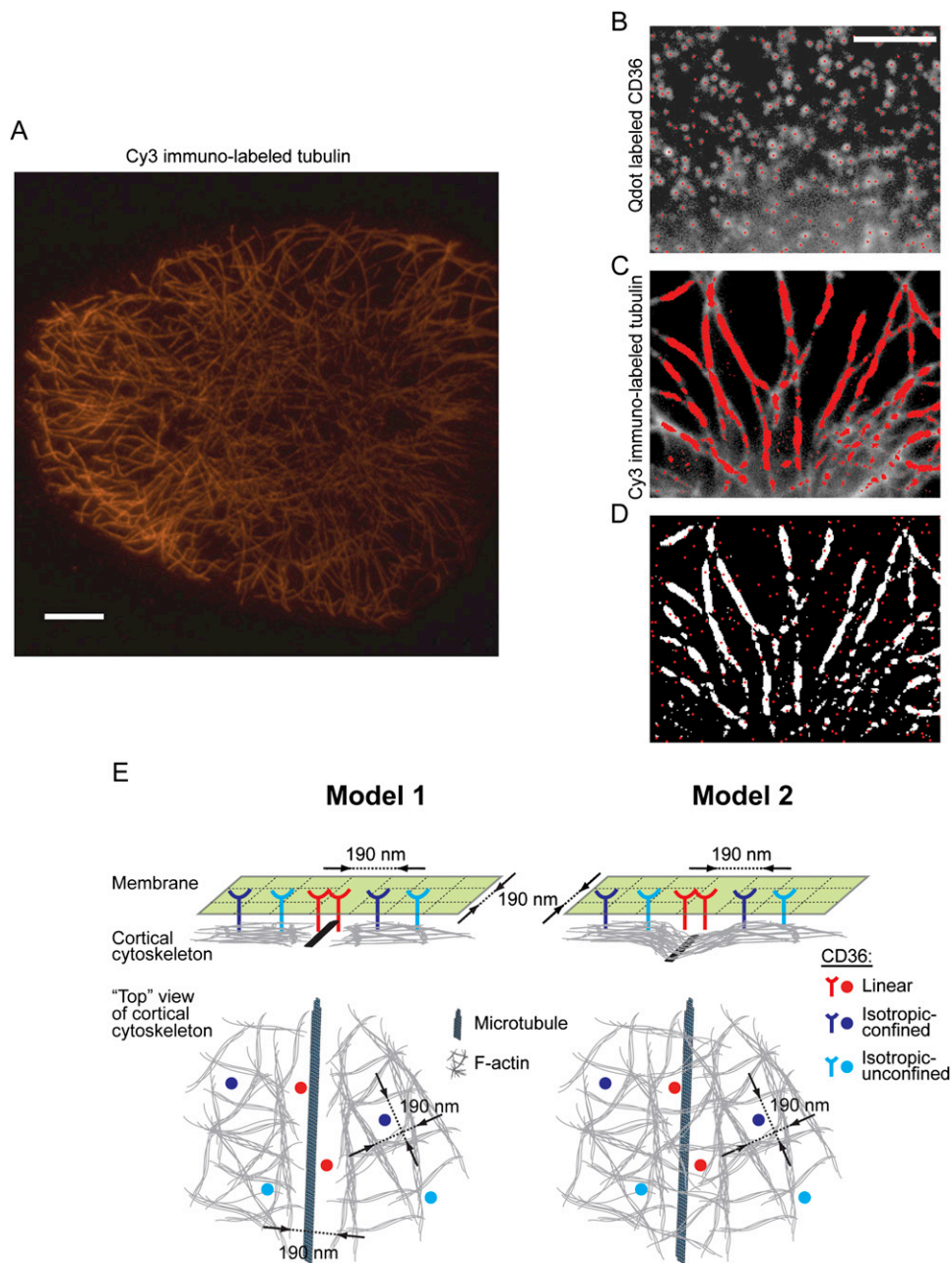


Figure S5. CD36 Linear Motion Depends on Microtubules, Related to Figure 6

(A) Total internal reflection fluorescence microscopy image of the ventral surface of a macrophage fixed with methanol, showing microtubules labeled with monoclonal anti-tubulin antibodies followed by Cy3-conjugated secondary antibodies. Scale bar, 10 μm .

(B–D) Analysis of two-color CD36 and microtubule fixed-cell images to calculate fraction of receptors colocalizing with microtubules. Image same as in Figure 6A.

(B) Qdot-labeled CD36 detected as point features. Scale bar (applicable to all images), 5 μm .

(C) Cy3-labeled microtubules detected as line features (Koller et al., 1995).

(D) Detected CD36 overlaid on detected microtubules. To ensure that the observed fraction was significant and did not result from coincidental colocalization due to the density of receptors and microtubules, we calculated the predicted coincidental colocalization fraction (Figure 6B) as follows: for each two-color image, we (i) replaced the original CD36 particles with the same number of particles but randomly placed throughout the image, (ii) calculated the fraction of random particle positions colocalizing with microtubules, and (iii) repeated (i) and (ii) 200 times to calculate the average coincidental colocalization fraction. The resulting fraction of coincidental colocalization (Figure 6B) was found to be significantly smaller than the experimentally observed fraction, confirming that the experimentally observed fraction of $27\% \pm 1\%$ was significant.

(E) Two models for cytoskeletal regulation of CD36 diffusion in membrane. Top panels are a “side” view showing the membrane, receptors and cortical cytoskeleton. Receptors are drawn to reach from the membrane to the cytoskeleton to depict indirect interactions between CD36 and actin. Bottom panels are a “top” view showing details of the cortical cytoskeleton and receptor positions. In both models, the designation of isotropic receptors as confined or unconfined

is arbitrary. Model 1: in regions without microtubules, the submembranous actin meshwork is isotropic, with roughly a repeat unit of 190 nm. In these regions, receptors can diffuse isotropically, and, likely due to CD36-integrin interactions (Figure S7), would get slowed down and often trapped within isotropic actin-delimited compartments. On the other hand, where microtubules become apposed to the membrane, they disrupt the integrity of the submembranous actomyosin meshwork, generating channel-like structures along which CD36 would move relatively unobstructed. Model 2: the submembranous actin meshwork is isotropic everywhere, but in regions where there are microtubules the interactions between actin and microtubules locally detach the actin meshwork from the plasmalemma, generating linear patches of bare membrane where CD36 does not interact with the cytoskeleton (the red receptors do not reach the cytoskeleton in the "side" view) and thus its diffusion is unimpeded. In both models, the reversible interactions between CD36 and F-actin would lead to the observed bias of CD36 localization toward the channel edges (Figure S3C). A third model to explain the observed bias of CD36 localization toward the channel edges, namely movement on the surface of a 3D "tube," is excluded by intensity considerations (Figure S3D).

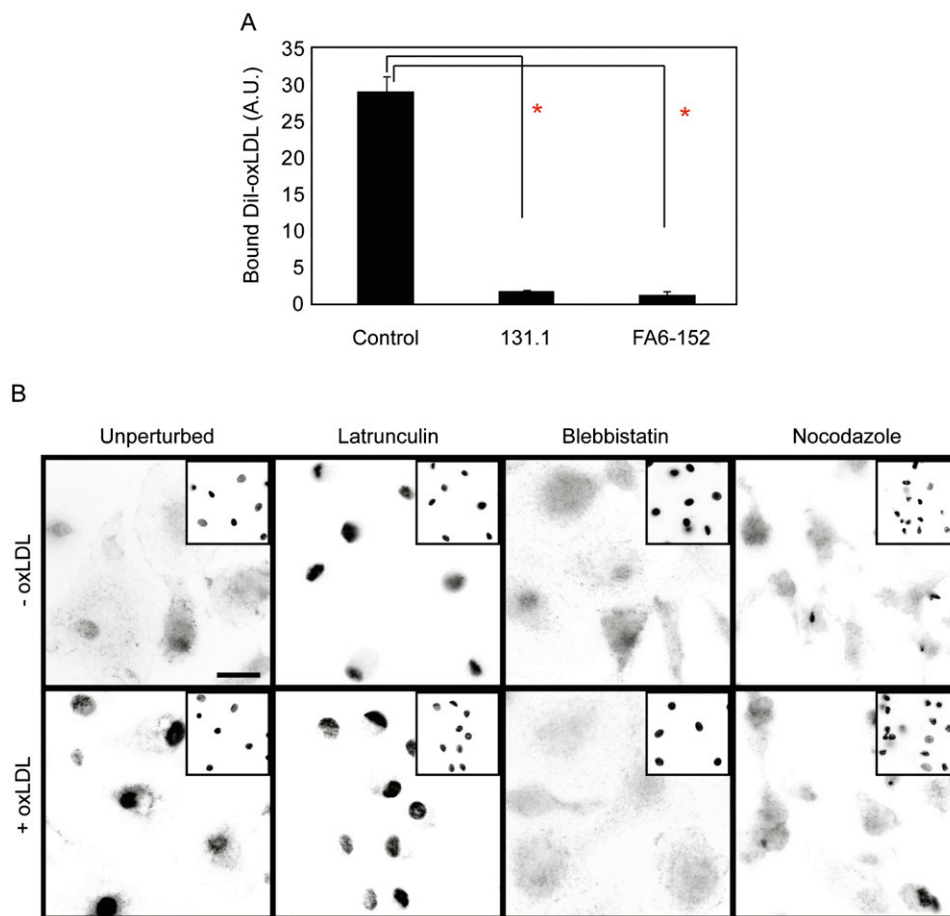


Figure S6. CD36 Linear Motion Enhances CD36 Function, Related to Figure 7

(A) Cells were treated without or with anti-CD36 antibodies 131.2 or FA6-152 prior to exposure to Dil-labeled oxLDL binding. Binding of the fluorescent conjugate was then determined by digital imaging. Data are means \pm standard errors of 3 determinations. * $p < 0.01$.

(B) Cells that had been otherwise untreated (unperturbed) or were pretreated as described above with latrunculin, blebbistatin or nocodazole were fixed and immunostained with antibody to phospho-cJun and counterstained with DAPI before (top row) or after treatment with oxLDL for 20 min at 37°C. Main panels show phospho-cJun labeling and insets are DAPI-stained samples. Images are representative of multiple fields from 3 similar experiments. Scale bar, 10 μ m.

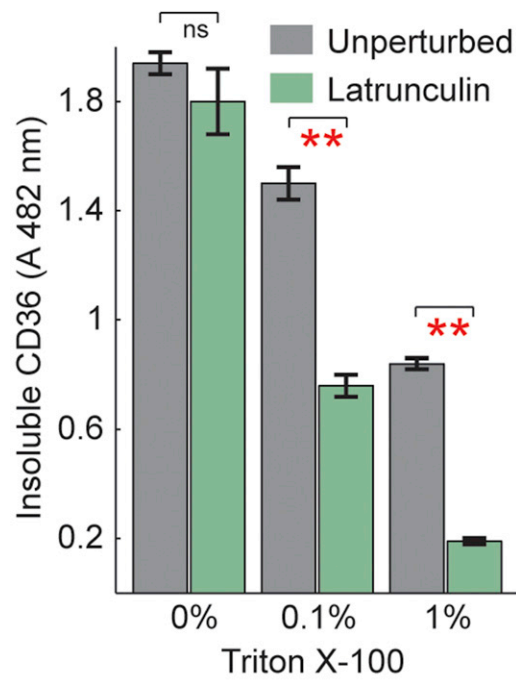


Figure S7. CD36 Interacts with F-actin, Related to Figure 5

Quantification of CD36 that remained insoluble following extraction with the indicated concentration of Triton X-100 in unperturbed (gray) and latrunculin-treated (green) differentiated U937 cells. Because of the large number of cells required for these biochemical experiments, we used differentiated U937 cells, a human macrophage line, instead of primary blood macrophages. Data are means \pm SEM from three independent experiments each. ** indicates p value $< 10^{-4}$, ns indicates not significant differences with p value > 0.1 .